SERI/STR--211-3609

DE89 009515

Research on Amorphous Silicon Based Thin Film Photovoltaic Devices

Task B: Research on Stable High-Efficiency, Large Area Amorphous Silicon Based Submodules

Annual Subcontract Report 16 March 1988 - 15 March 1989

A. E. Delahoy
F. B. Ellis, Jr.
F. J. Kampas
T. Tonon
H. A. Weakliem
Chronar Corporation
Princeton, New Jersey

December 1989

SERI Technical Monitor: W. Luft

Prepared under Subcontract No. ZB-7-06003-1

Solar Energy Research Institute
A Division of Midwest Research Institute

1617 Cole Boulevard
Golden, Colorado 80401-3393

Prepared for the
U.S. Department of Energy
Contract No. DE-AC02-83CH10093

PREFACE

This Annual Technical Progress Report covers research performed by Chronar Corporation during the period March 16, 1988 to March 15, 1989, under subcontract No. ZB-7-06003-1. This period represents the second year (Phase II) of a three year program. The program manager is Dr. Alan E. Delahoy. The contributors to research reported here are listed below:

Mr. J.A. Cambridge	
Mr. H. Chao	
Dr. A.E. Delahoy	Principal Investigator Subtask B1/B2
Dr. F.B. Ellis, Jr.	
Dr. E. Eser	
Mr. J. Esler	
Mr. H. Field	
Dr. S.C. Gau	
Mr. J. Houghton	
Ms. M. Johnson	
Mr. J. Kalina	
Dr. F.J. Kampas	Principal Investigator Subtask B3
Mr. C. Kothandaraman	
Mr. L. Michalski	
Mr. A. Nagy	
Mr. F. Ramos	
Mr. A. Savary	
Dr. H. Schade	
Mr. W. Stroud	
Dr. T. Tonon	
Mr. K. Urbanik	
Mr. R. Vos	
Dr. H.A. Weakliem	

In addition, we express our thanks to Dr. Isaac Balberg, The Hebrew University, Jerusalem, for diffusion length studies based on the steady-state photocarrier grating technique.

NOTICE

Printed in the United States of America
Available from:
National Technical Information Service
U.S. Department of Commerce
5285 Port Royal Road
Springfield, VA 22161

Price: Microfiche A01
Printed Copy A04

Codes are used for pricing all publications. The code is determined by the number of pages in the publication. Information pertaining to the pricing codes can be found in the current issue of the following publications which are generally available in most libraries: *Energy Research Abstracts (ERA)*; *Government Reports Announcements* and Index (*GRA* and I); *Scientific and Technical Abstract Reports (STAR)*; and publication NTIS-PR-360 available from NTIS at the above address.

TABLE OF CONTENTS

LIST OF FIGURES

LIST OF TABLES

SUMMARY

Objective

The primary objective of this subcontract is to develop amorphous silicon p-i-n/p-i-n tandem junction photovoltaic submodules ($\geq$ 900 cm^2) having an aperture area efficiency of at least 9%. A further objective is to demonstrate 8% tandem submodules that degrade by no more than 5% under standard light soaking conditions.

Discussion

Useful progress was made during Phase II in raising the 1 cm^2 tandem cell efficiency from 7.8% to 8.7%, and in raising the power output of 1 sq.ft. tandem submodules from 5.5 watts to 6.0 watts (7.2% aperture area efficiency).

The increase in cell efficiency resulted mainly from careful optimization of the tandem a-Si/a-Si deposition conditions, with particular attention being paid to the central n_1/p_2 tunnel junction. Here it was discovered that insertion of a TiO_x recombination layer could improve both open-circuit voltage and fill factor.

Transport and defect states in a-Si:H were studied using a variety of techniques, including the steady state photocarrier grating technique and current DLTS applied to p-i-n devices.

Submodule fabrication was accomplished using laser scribing for all three constituent layers (SnO_2, a-Si:H, Al). In order to realize the latent performance of the basic a-Si/a-Si structure, it was found necessary to subject the submodules to two distinct steps of post-fabrication defect removal. These steps were electrical and chemical in nature.

The groundwork was laid for further efficiency advances through research concerning the minimization of optical losses and new module designs, as described below.

A comprehensive study of the deposition of SiO_2 barrier layers to improve the conductivity of the subsequently deposited SnO_2 will enable more transmissive SnO_2 (for a given sheet resistance) to be made available for use in Phase III.

Of considerable significance was the successful development of high quality, doped films of ZnO by magnetron sputtering. Conductivities of 2500 S/cm were achieved, corresponding to a sheet resistance of 5.4 ohms/sq. for a film thickness of 0.75μm. Various back reflectors involving ZnO were evaluated, but final details have yet to be worked out.

The almost total elimination of reflection from alkali-borosilicate glass was demonstrated after formation of a graded-index surface layer. Tin oxide deposition was successfully integrated into this scheme, and devices exhibiting higher peak quantum efficiencies were prepared on graded index layer/glass/SnO_2 substrates.

Some experimental work was performed to realize demonstration submodules employing two levels of metallization, features being 98% area utilization and reduced electrical losses (dot contact modules).

The fabrication of efficient p-i-n cells on ZnO substrates was found to be non-trivial. Successful procedures were developed, however, enabling an efficiency of 8.3% to be achieved during Phase II. The ability to employ a transparent conductor other than SnO_2 opens up many avenues for future research, including the prospect of improved efficiency and stability.

Long term light soaking studies designed to compare the performance of tandem cells and single junction cells indicate that, at their present respective stages of development, the stabilized efficiency of tandem cells exceeds that of single junction cells by about 10%. Outdoor exposure of a glass-encapsulated 1 sq.ft. tandem submodule for 271 days resulted in a net drop in power output of 13%.

Conclusions

- An improved set of deposition conditions was established for tandem cells resulting in initial efficiencies almost equal to those of single junction cells.
- A 1 sq.ft. a-Si/a-Si tandem submodule has been fabricated having an aperture area efficiency of 7.2%.
- Good outdoor stability was observed for an encapsulated tandem submodule.
- High quality doped zinc oxide films (5 ohms/sq.) have been produced by magnetron sputtering.
- Successful development in Phase III of granular ZnO, a viable back reflector scheme, and low-loss module designs will enable the primary objectives to be attained.

SECTION 1.0

INTRODUCTION

This research program is designed to advance the state-of-the-art in a-Si:H photovoltaic submodule performance. The research encompasses both single and tandem junction submodules in 1 sq.ft. or 1 x 3 sq.ft. sizes, with specific goals for efficiency and stability. From Phase II (roughly FY88) onwards, the emphasis has been, and will continue to be, placed on tandem devices because of indications of their superior stability.

The research is divided into three fields (subtasks B1, B2, and B3), as follows:

B1. Semiconductor Materials and Small Area Cells. The objectives here include the deposition of amorphous silicon materials over large areas, the optimization of these materials as guided by physical, chemical, electrical and optical characterization, and the optimization of the efficiency and stability of small area p-i-n and p-i-n/p-i-n cells.

B2. Non-Semiconductor Materials. Here the objectives are the deposition of front and back contact materials (transparent conductors and metallization) over large areas, the development of advanced back reflectors, minimization of optical losses, and study of the thermal stability of the associated materials and interfaces.

B3. Submodules. The objectives here are the fabrication and optimization of large area interconnected devices on a monolithic substrate. This includes investigation of submodule configurations and patterning approaches, increase of active area, defect-analysis, and a comparison of the light soak behavior of single and tandem junction submodules.

The main findings and results established during Phase II are described below. They are categorized according to the appropriate subtask.

SECTION 2.0

SEMICONDUCTOR MATERIALS AND SMALL AREA CELLS

2.1 I-LAYER ANALYSIS

This section describes techniques we have used for the characterization of a-Si:H i-layers. Since it is desirable to be able to correlate these results with cell performance, we have concentrated on developing methods that are applicable to completed p-i-n solar cell structures. Of particular interest is the change in material and device parameters as a function of light soaking. The i-layer properties that we have measured are:

- density of states (by thermally stimulated currents (TSC) and deep level transient spectroscopy (DLTS),
- mobility-lifetime product of electrons and holes (by charge collection), and
- ambipolar diffusion length (by the steady state photocarrier grating technique).

2.11 Density of States

Thermally stimulated current measurements have frequently been applied to determine trapping levels in crystalline silicon junction devices, but only in a few instances to characterize a-Si:H, either by using undoped layers or Schottky barrier diodes. We have performed such measurements on a-Si:H p-i-n diodes [1]. The sample is held in a vacuum dewar, and after first filling the traps by optical excitation at low temperature, the short-circuit current of the sample is monitored while heating at a constant rate (0.3 degrees/s). We find a prominent low temperature peak and a broad distribution of states at higher temperatures. Roughly speaking, the energy depth of the trap E_t is related to the temperature T_m of a TSC peak by the relation $E_t = 25\ kT_m$. Upon light soaking the low energy peak is reduced while the high energy peak is considerably increased. By integrating the charge released from states with depth 0.35 - 0.75eV, which we believe to represent defect states, we have estimated the number of defect states in the as-deposited sample to be $5 \times 10^{15}\ cm^{-3}$. After light soaking at 10 suns for 1 hour, the number of defect states in this energy range rose to $5 \times 10^{16}\ cm^{-3}$ [2].

We are able to directly correlate solar cell performance with defect concentration by means of the following experiments [2]. For each of several p-i-n cells, we measured the TSC spectrum and low intensity (0.01 sun) fill factor at various levels of light-induced degradation. Since in the collection length model the collection length to i-layer thickness ratio (L_{co}/L) is inversely proportional to defect concentration, we converted the FF data to L_{co}/L and plotted it versus defect concentration (log plot). This plot is shown in Fig. 1 which confirms the inverse proportionality of these quantities.

Later work based on current DLTS also showed this inverse relationship of L_{co}/L and defect concentration for a given sample, but a unique relationship between these quantities did not exist for all samples. It was conjectured that this non-uniqueness resulted from field distortion in the i-layer.

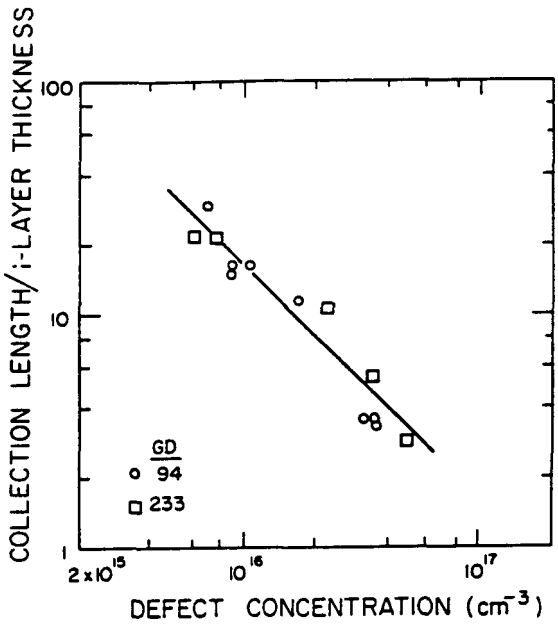

Fig. 1 Inverse proportionality between the collection length/i-layer thickness ratio and defect concentration for glow discharge deposited p-i-n cells.

2.12 Mobility-Lifetime Product of Holes and Electrons

By analyzing charge collection versus reverse bias for a 10μm thick p-i-n structure illuminated with strongly absorbed light through the p and n layers we have determined the mobility-lifetime ($\mu\tau$) product for both holes and electrons [3]. The data is shown in Fig. 2. Light of low intensity was used in order to avoid distortion of the electric field by the space charge of the photogenerated carriers. In the absence of space charge the single carrier current is then

$$J = J_o \, L_d/L \, [1 - \exp(-L/L_d)]$$

where J_o is the saturated current, $L_d = \mu\tau E$ is the drift length, and L is the i-layer thickness. The curve in Fig. 2 for electrons follows this expression, as does the curve for holes for sufficiently large bias. Our results are:

$$\mu\tau \text{ (hole)} = 3.0 \times 10^{-8} \text{ cm}^2/\text{V}$$

$$\mu\tau \text{ (electron)} = 3.6 \times 10^{-7} \text{ cm}^2/\text{V}$$

At low voltages, the data in Fig. 2 for hole transport (strongly absorbed light incident on the n-layer) exhibits the J-V behavior for a single carrier space charge limited current, namely

$$J_{sp\ ch} = \epsilon \mu_d V^2/L^3$$

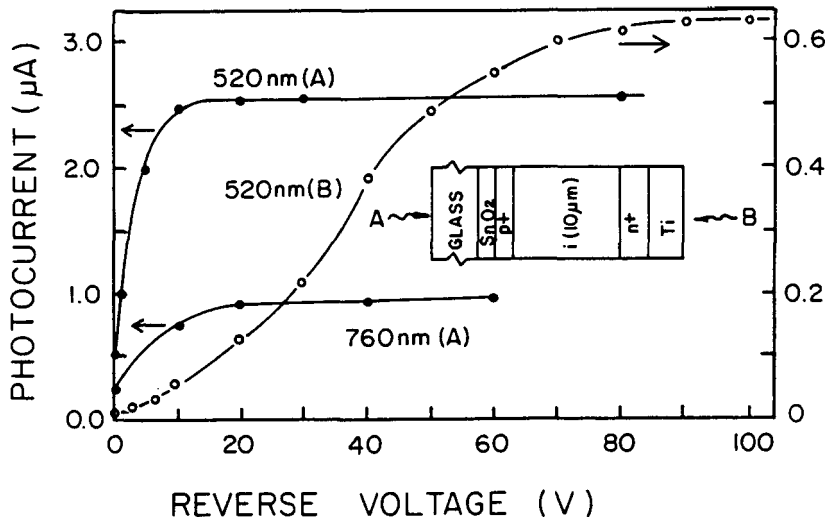

Fig. 2 Charge collection in a p-i-n structure as a function of reverse bias, with light incident through either the n or p-layer; the i-layer of this structure is 10μm thick.

2.121 Implications for Photovoltaic Behavior

It is interesting to note that the J-V curve in Fig. 2 for uniformly absorbed light has a shape almost identical to that for the electron transport case and is quite unlike the hole transport curve. This suggests that the carrier with the shorter drift length does not determine the photovoltaic J-V curve, as is often intuitively assumed. It further agrees with the two-carrier uniform field model in which the relevant parameter is the sum of the electron and hole drift lengths [4].

2.13 Ambipolar Diffusion Length

One of the most important parameters determining the performance of p-i-n cells is the minority carrier diffusion length L_m. Historically, this parameter has been measured only on single i-layers, and therefore may not apply to completed p-i-n structures prepared in a single chamber deposition system. We have applied the steady-state photocarrier grating technique [5,6] which measures the ambipolar diffusion length L (roughly $\sqrt{2}L_m$ in a-Si:H) to i-n, p-i, and p-i-n structures [7,8]. Fig. 3 shows the light intensity dependence of L for an i-layer, a p-i structure, and a light soaked i-layer [7]. Note that the p-i structure possesses a larger value of the ambipolar diffusion length than the single i-layer. It was also shown that, as a rule of thumb, the real L value of the i layer in a p-i-n structure is typically 10-20% higher than the value measured directly on such structures [8].

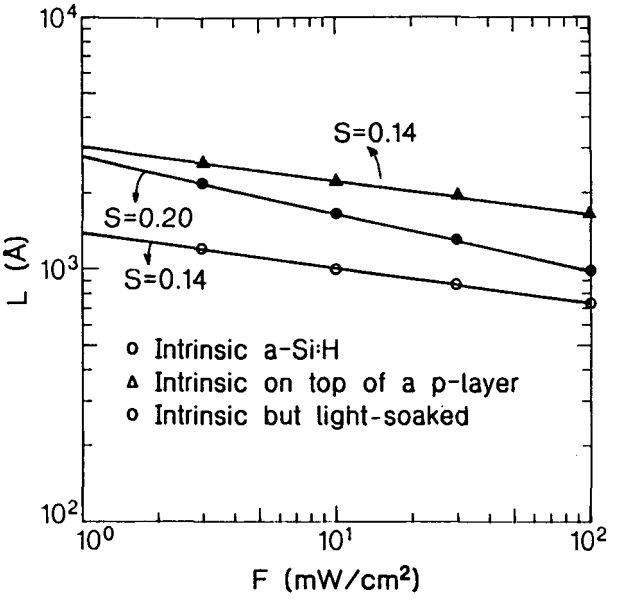

Fig. 3 Ambipolar diffusion length as a function of incident light intensity for three systems: a-Si:H i-layer, p-i structure, and light-soaked i-layer.

2.2 SEMICONDUCTOR MATERIALS

For the most part, our standard i- and n-layers were employed without modification during Phase II. These layers are:

- a-Si:H i-layer (prepared from a SiH_4/H_2 mixture)
- a-$SiH_{1-x}C_x$:H transitional i-layer (SiH_4,CH_4,H_2)
- a-Si:H n-layer (SiH_4, H_2, PH_3)
- μc-Si:H n-layer (SiH_4, H_2, PH_3; high RF power)

On the other hand, a new type of silicon-carbide p-layer was developed, and has been adopted as a standard. Work was also performed in the area of (p-i) transitional i-layers (buffer layers). These layers are described below. Further optimization of the n_1 and p_2 layers in tandem cells are described in Section 2.3.

2.21 Carbon-Graded P-Layers

With the motivation of producing a photovoltaically-active p-layer, band gap graded a-$Si_{1-x}C_x$:H p-layers were investigated. The carbon source was methane (CH_4). To produce the carbon-graded p-layer, the CH_4 flow was continuously reduced during p-layer deposition. The incorporation of such carbon-graded p-layers into p-i-n devices resulted in an improvement of J_{sc} by 1mA/cm^2 as a result of excellent blue response. The spectral response of devices employing the new and old p-layers are compared in Fig. 4. Further work to improve the V_{oc} obtained with these p-layers must be undertaken, since at present the average V_{oc} is about 0.83V.

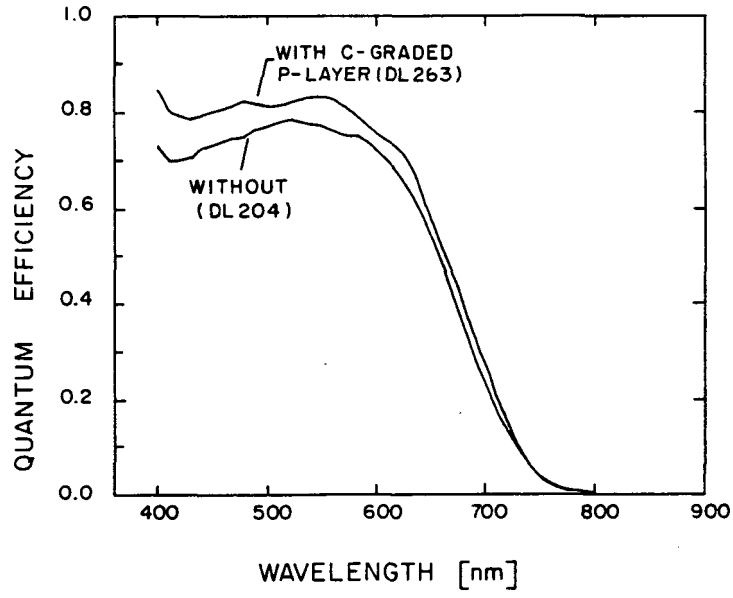

Fig. 4 Spectral response of p-i-n cells with carbon-graded and noncarbon-graded a-$Si_{1-x}C_x$:H p-layers.

2.22 Transitional I-layers

Very high open-circuit voltages (up to 0.93V) have been obtained through the substitution of Si_2H_6 for SiH_4 in our usual transitional i-layer feedstock gas mixture. These high V_{OC}'s were usually accompanied by relatively low (0.58) fill factors, and efficiency gains have not yet been realized.

2.3 TANDEM CELL DESIGN AND OPTIMIZATION

Device work performed under this subcontract has slowly shifted to an emphasis on same bandgap, tandem junction a-Si:H cells and submodules, because of their superior stability. We had previously argued that, because of optical absorption in the central n_1/p_2 junction, tandem cells could never equal single junction cells in initial (as-deposited) conversion efficiency. We now believe this argument to have been flawed, the reason being that the greater number of degrees of freedom in tandem cell design allows for compensating increases in open-circuit voltage and fill factor. It thus appears that tandem cells can be built having initial efficiencies equal to those of optimized single junction cells, and consequently having stabilized efficiencies higher than those of single junction cells.

The structure of the tandem cells discussed in Section 2.3 is glasglass/SnO_2/ p_1-i_{t1}-i_1-n_1/p_2-i_{t2}-i_2-n_2/Al. The i_{t1} and i_{t2} layers are undoped, band gap graded, amorphous silicon carbide transitional i-layers. We discuss below some of the properties of tandem cells, and areas which we found important in their optimization. (In this section, "optimized" means optimized for initial conversion efficiency).

2.31 Thickness of I_2-Layers

It is well known that in single junction cells, fill factor decreases with increasing light intensity. It would thus appear that, since the i_2-layer of a tandem cell receives approximately half the light of a single junction cell, the i_2-layer could be made thicker than the optimized thickness of a single cell (in order to absorb more light) while maintaining a high fill factor. This is borne out experimentally, and we find that tandem cells optimized for initial efficiency have i_2 layers 20% thicker than the i-layer of our optimized single junction cells (i-layer thicknesses 0.7 and 0.5 μm, respectively).

2.32 Current Matching

If the photocurrents J_1 and J_2 generated by the top and bottom stacks of a tandem cell are unequal, then the short-circuit current of the cell will be clamped to a value given by the illuminated I-V characteristic of the current-limiting cell, i.e. to the lower of the two photocurrents.

Since for a cell of fixed total thickness the sum of these two photocurrents is a constant equal to the total integrated optical absorption $J_1 + J_2 = J_{tot}$ the maximum J_{sc} is obtained when the two photocurrents are equal i.e. $J_1 = J_2$.

The photocurrents J_1 and J_2 for a tandem cell can be determined by integrating (for both stacks) the product of the individual external quantum efficiencies and the solar photon flux. (The quantum efficiencies can be obtained by spectral response measurements performed under appropriate voltage and light bias conditions).

In this way it can be determined experimentally whether a tandem cell is matched, or to what degree the cell is top or bottom stack limited. Depending on the overall thickness of the cell, the matched condition is typically achieved for i_1:i_2 thickness ratios of between 1:5 to 1:9.

We have observed that, if under a given spectrum of illumination a tandem cell is top limited ($J_1<J_2$), then a characteristic step appears in the reverse bias portion of its I-V curve. This is illustrated in Fig. 5. The solid curve is the I-V characteristic of of a tandem cell illuminated by the (blue-deficient) light of an ELH lamp, causing it to be top limited. Two photocurrent plateaus are found, one near short-circuit, the other under sufficient reverse bias. These plateaus, we claim, represent J_1 and J_2. (Mechanisms by which the full current J_2 from the bottom stack can be driven through the top stack have been discussed in our semiannual report [3].) Confirmation of this claim is provided by the results of the following two experiments. Upon the addition of red light, the I-V curve given by the dashed line was obtained. Note that the ratio of the increase in the two photocurrent levels is about 4, somewhat less than the i_2/i_1 thickness ratio for this cell of 5.7, but correctly representing the incremental absorbed light in the two i layers. Upon the addition of blue light, largely absorbed by the top stack, the postulated J_1 and J_2 photocurrent levels increase by a large amount and small amount respectively, as would be expected. Note that the blue light was just sufficient to eliminate the characteristic step in the I-V curve. This telltale step is therefore recognized as a signature of top stack limitation.

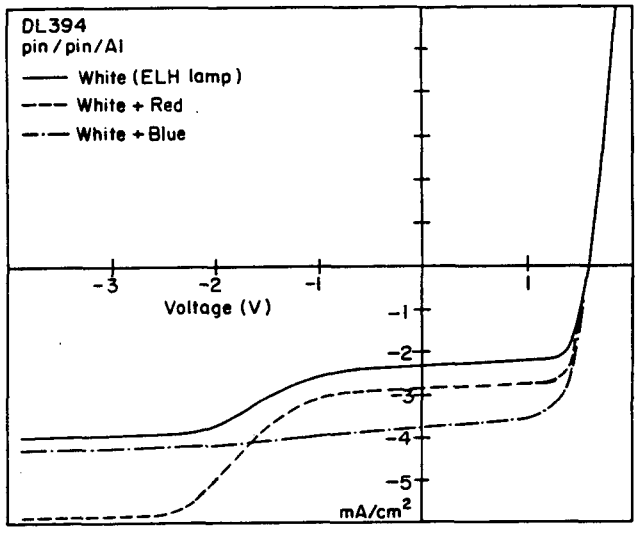

Fig. 5 Demonstration that the appearance of two photocurrent plateaus in tandem cells is a signature of top stack limitation.

For a given thickness of the i_2-layer, the thickness of the i_1-layer that yields the matched condition $J_1 = J_2$ can be found as follows. Define a mismatch parameter β to be

$$\beta = \frac{J_1 - J_2}{J_1 + J_2} \times 100\%$$

Then a plot of deposition times β versus t_1 for cells prepared with different i_1-layer t_1 yields the correct i_1-layer thickness for current matching when β=0. This is illustrated in Fig. 6 for cells prepared with a constant i_1-layer deposition time of 110 minutes.

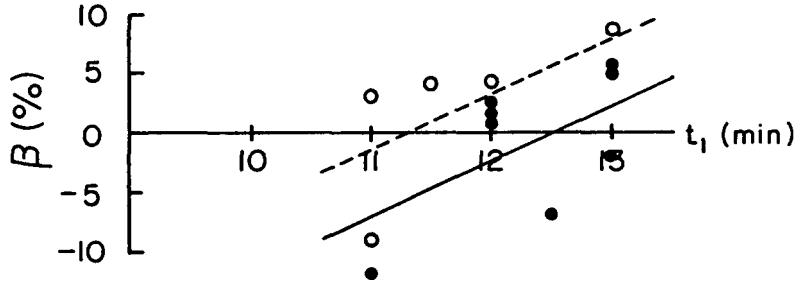

Fig. 6 Plot of mismatch parameter β versus i_1-layer deposition time for tandem cells.

Fig. 6 indicates that an i_1 deposition time of 12.5 minutes is the best choice for current matching. Circled points represent data for cells having a TiO_x recombination layer inserted between the n_1 and p_2 layers. It is clear from Fig. 6 that this tends to increase β presumably by both increasing the current generated by the top stack (by reflection) and decreasing the current from the bottom stack (by reflection and absorption), so that the best choice of i_1 time for such cells is now 11.25 minutes. By constructing a family of such mismatch plots for various i_2-layer deposition times, we have been able to generate a figure which shows the optimized i_1 time for current matching versus i_2 time.

2.33 The N_1/P_2 Tunnel Junction

We have found that the shape of the a-Si:H/a-Si:H tandem cell I-V curve near V_{OC} is strongly influenced by the properties of the central n_1/p_2 tunnel junction. In particular, we discovered that inflection points near V_{OC}, or a high diode forward resistance, can be avoided by increasing the doping of the n_1 and p_2 layers.

2.331 Effect of a TiO_x Recombination Layer

A further interesting discovery was that deposition of TiO_x (a conductive sub-oxide of Ti, see Section 3.3) following the n_1 layer and prior to the p_2 layer, is capable of improving both the open-circuit voltage and fill factor of tandem cells with only an insignificant reduction in current through optical absorption. The TiO_x layer also tends to prevent the occurrence of kinks in the I-V curve near the V_{OC} point.

The dependence of V_{OC} on the thickness of the TiO_x layer is shown in Fig. 7. While we do not yet understand the origin of the scatter in the data, it is nevertheless clear that TiO_x is capable of improving V_{OC} by 40-50 mV.

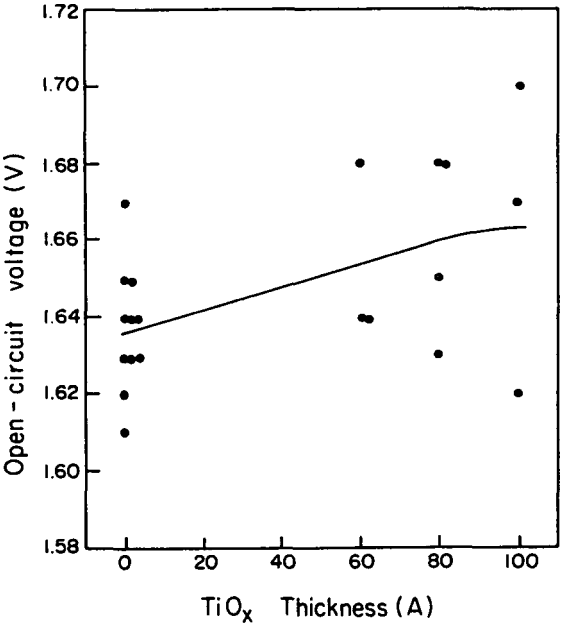

Fig. 7 Open circuit voltage versus TiO_x thickness for tandem cells having a TiO_x recombination layer between the top and bottom stacks.

Fig. 8 shows that the increase in FF is even more pronounced, but in this case there appears to be an optimum TiO_x thickness (about 80Å) most likely resulting from the series resistance of TiO_x films that are too thick. The data plotted in these two figures are the average V_{oc} and FF for dot cells deposited over an entire 1 ft.sq. plate. Note the very high average dot fill factor (0.768) that was obtained in one run with TiO_x.

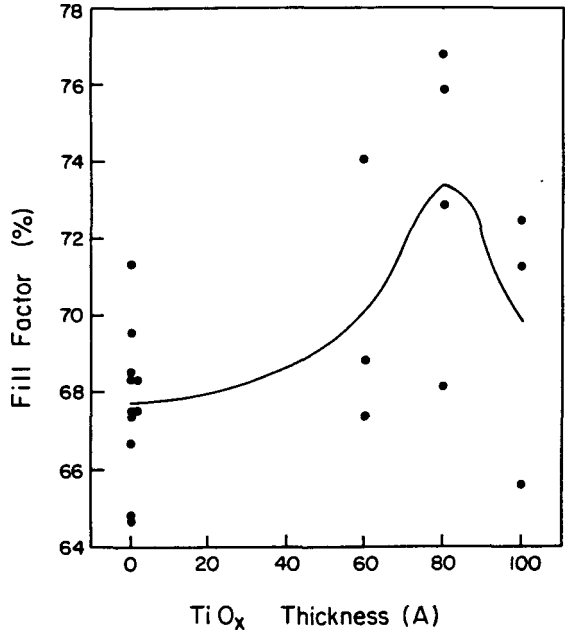

Fig. 8 Fill factor versus TiO_x thickness.

We also found that the slight loss in current through optical absorption in the TiO_x can be regained by reducing the thickness of the p_2 layer, a procedure which would normally lead to a reduction in V_{oc}.

The origin of the remarkable increase in fill factor is to some extent clarified by Fig. 9, which compares the I-V characteristics of cells with and without the TiO_x layer, but which are otherwise identical except for a reduced p_2 thickness in the cell containing the TiO_x. The V_{oc} and FF of the two cells are 1.66V and 0.746, and 1.61V and 0.708, respectively. It can be seen that the effect of the TiO_x layer is to considerably reduce the forward diode resistance of the cells, dV/dJ at V_{oc} being 15.3 ohm cm^2 for the cell with TiO_x, and 34.0 ohm cm^2 for the cell without. No change in the conductance near V = 0 was observed. It would appear that the TiO_x facilitates electron-hole recombination at the n_1/p_2 interface. If this is so, then the improvement in V_{oc} may be due to the suppression of a reverse photovoltage generated by the n_1/p_2 junction.

2.34 Modification of the transitional I-Layer

The lower current density in tandem cells should allow a higher carbon content in the transitional i-layers before unacceptable series resistance losses are encountered. Thus, both higher methane flows and longer deposition times were incorporated in the transitional i-layer optimization process in order to increase V_{oc}.

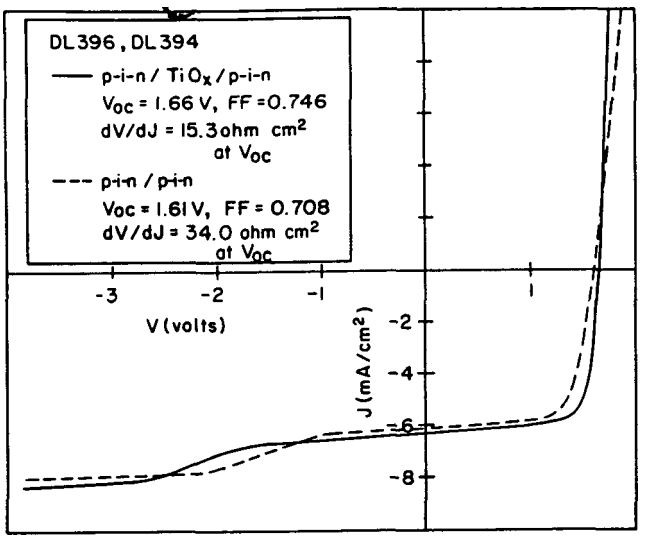

Fig. 9 Illuminated J-V curves for tandem cells showing the increase in V_{OC} and FF through incorporation of the TiO_x layer. (For this figure, spectrum of light is not that of sunlight but is blue-deficient)

2.4 HIGHEST PERFORMANCE CELLS

2.41 Single Junction Cells

We have in the past constructed a 10% 1 cm^2 cell employing an evaporated Ag back contact. Because of the unreliable nature of such contacts we are currently seeking to develop a conductive oxide/metal reflector type contact (see Section 3.4). Using a simple Al contact we have achieved a 9.5% 1 cm^2 single junction cell. The substrate for this cell was soda lime glass/SiO_2/SnO_2:F, whereas our standard substrate is soda lime glass/SnO_2:F. Unfortunately, tin oxide glass with the SiO_2 diffusion barrier has generally not been available for this work, despite indications that it is a superior substrate. For example average dot efficiency in run DL340 on standard SnO_2 was 8.8% compared to 9.5% for cells on SiO_2/SnO_2. The I-V curve for the 9.5% 1 cm^2 cell is shown in reference 3. In the future we expect to employ both SiO_2/SnO_2 and ZnO as substrate materials.

2.42 Tandem Junction Cells

Steady advances in tandem cell efficiency have been made during this subcontract, as shown in Table I (in-house data). The progress has resulted largely from changes made in the deposition of the a-Si:H layers, and from the introduction of the TiO_x recombination layer, as described in Section 2.331 above.

The J-V curves of our best 0.08 cm^2 and 1.0 cm^2 tandem cell (9.3% and 8.7%) are shown in Figs. 10 and 11, and the cells employ TiO_x layers of thickness 80A and 100A, respectively. Glass having a graded index of refraction AR coating (see Section 3.1) was employed as the substrate for the 9.3% cell. Measurements performed by SERI on a 1 cm^2 tandem cell from run DL387 yielded an efficiency of 8.5%.

Table I. Progress in Tandem Cell Efficiency		
	$0.08cm^2$	$1.0cm^2$
Phase I	8.3%	7.8%
Phase II 6m	8.7%	8.2%
12m	9.3%	8.7%

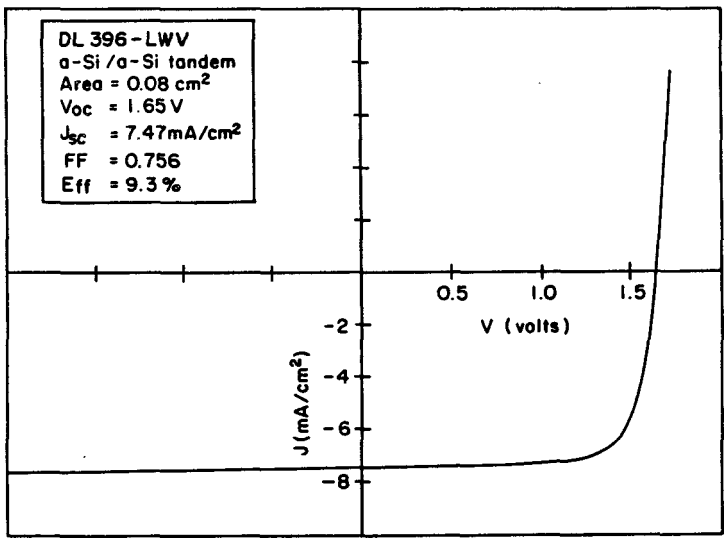

Fig. 10 J-V curve for a 9.3% tandem cell formed on graded-index pyrex and with TiO_x recombination layer. Note the high fill factor (0.756).

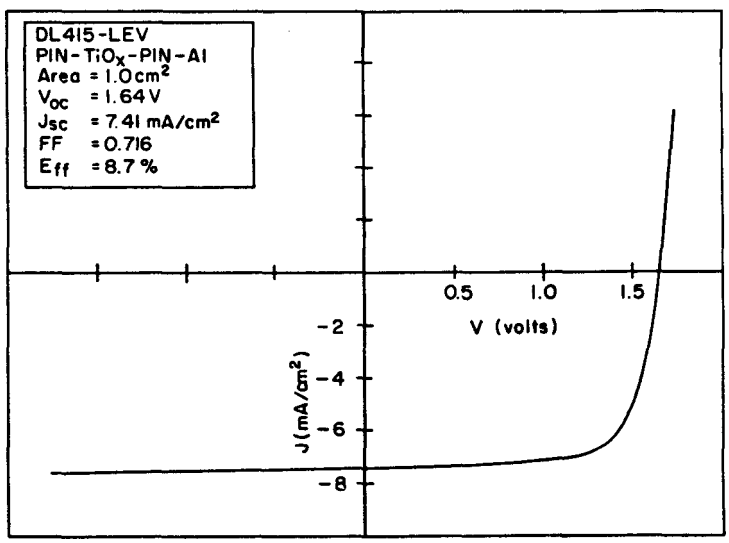

Fig. 11 J-V curve for a 8.7% $1cm^2$ tandem cell.

2.5 NOVEL CELL STRUCTURES

2.51 PINP Cells

In connection with the ITO back reflector program, several runs were performed to give cells having the structure p-i-n-p. The intent of this work was to improve the contact resistance between the doped layer and the ITO. These runs always performed well with Al metallization, e.g. run DL351 gave average dot parameters: 0.84V, 15.0 mA/cm^2, FF 0.69, Eff 8.7%. In the case of Ag and ITO/Ag metallization, cells having the extra p layer usually yielded fill factors higher than those prepared on standard p-i-n material (see Section 3.41).

2.52 PININ Cells

It is well known that in order to increase the photostability of p-i-n cells, the i-layer must be made thin, for example from 0.2 to 0.35 μm. However, manufacturing yield can be adversely affected by the use of very thin (0.2μm) i-layers. As a possible solution to this problem we invented the p-i-n-i-n cell. The p-i-n section of this cell is photovoltaically active, while the back n-i-n structure serves as a passive contact. We fabricated such cells having 0.2μm thick front and back i-layers, for a total thickness of 0.4μm. This type of cell might be expected to posses the stability of a 0.2μm p-i-n cell, but possess the higher manufacturing yield (for 1 ft.sq., or larger, submodules) of a 0.4μm cell. The as-deposited average dot parameters were 0.84V, 10.5 mA/cm^2, FF 0.71, Eff 6.3%. The stability of these cells is examined in Section 2.61.

2.6 STABILITY

Several earlier studies of ours have demonstrated the superior photostability of tandem devices relative to single junction devices. In our paper presented at the 8th European PV Conference [9], for example, we reported that a tandem junction cell held the record as being (under a Na lamp) the most stable cell among a group that was light soaked for 2.4 years. Indeed, its efficiency loss was 23% compared to one particular single junction cell whose loss was 34%. However, the starting efficiency of the single junction cell was considerably higher, and its final (stabilized) efficiency was 5.44% compared to 5.05% for the tandem cell. One might therefore conclude that for practical applications the single junction cell would still be preferable. Yet, now that our tandem cell expertise is greatly improved, starting efficiencies for tandems are comparable to those of single junction cells. We therefore recognized a need to perform a new round of stability tests designed to be an accurate, fair, and realistic comparison of state-of-the-art single and tandem junction cells.

2.61 Comparison of Various Cell Types

To accomplish the above tests, we designed and built a special turntable that rotates under a metal halide lamp and reflector, and which can accommodate up to 36 diagnostic cells arranged in a circle. By this means we ensure that each cell receives exactly the same light dose. The turntable is fitted with contacts and potentiometers, so that the cells can be maintained at a known load point. In order for the tests to be as realistic as possible we decided to adopt the following experimental conditions:

1. Cells individually loaded close to their maximum power point.

2. Irradiation 0.95 suns.

3. Cell temperature 50°C.

We have completed the first study using this turntable. Two cells from ten different runs were employed. A total of 8 sets of J-V measurements were made, ranging from 0 to 1230 hours of light soaking. The soak temperature was 30 C for the first 400 hours, 70 C for the next 160 hours, and 50 C for the final 670 hours. The data is given in condensed form in Table II. Here only initial and final efficiencies are given, and the entries are the average efficiencies for the two cells of each run. The cells are listed according to their stability ranking. The following observations were made:

1. The four most stable cells are tandem-junction cells.

2. The least stable cell is the 0.5μm single junction cell.

3. For both single and tandem-junction cells, stability improves with decreasing i- or i_1- layer thickness.

4. The five highest final efficiencies were achieved by tandem cells.

5. Tandem cells with i_1-layer thickness of 0.6μm are as stable as single junction cells having an i-layer thickness of 0.35μm.

Table II. Stability ranking for single and tandem junction cells light soaked at 0.95 suns for 1230 hours.

Run #	Type of cell	Key conditions[a]	Efficiency(%)		Percent change (%)	Stability ranking
			Initial	Final		
394	Tandem	10.5/60	7.94	6.05	23.8	1
396	Tandem	10.5/60 TiO_x	8.24	6.19	24.9	2
398	Tandem	12.5/80	7.61	5.66	25.6	3
393	Tandem	11/110	7.66	5.57	27.3	4
314	Single	0.25	7.35	5.32	27.6	5
327	Single	0.35	7.88	5.66	28.2	2
391	Single[b]	0.2/0.2	7.55	5.36	29.0	7
380	Tandem	12/110 TiO_x	8.12	5.72	29.6	8
385	Tandem	13/110 TiO_x	8.50	6.00	29.9	9
383	Single	0.5	7.78	4.87	37.4	10

a) i_1/i_2 layer times (min) or i-layer thickness (μm); (110 min $\sim$ 0.7 μm); presence of TiO_x recombination layer indicated

b) p-i-n-i-n structure

We have continued to monitor some of these cells, and it is noteworthy that the two tandem cells of run 396 still average an efficiency of 6.00% after a total of 1950 hours irradiation.

In conclusion, this study shows that, after 1200 hours of light soaking (equivalent to about 8 months of outdoor exposure), a final efficiency advantage of about 10% accrues to thin tandem junction cells relative to thin single junction cells. Future studies will examine the performance of even thinner tandem cells, the influence (if any) of a ZnO substrate, the very long term approach to stabilization, and the dependence of stabilized efficiency on operating temperature.

2.62 Possible wavelength effect in light soaking

It had occurred to us that one possible reason for the superior stability of tandem cells compared to single junction cells (apart from the reduced intensity seen by the bottom stack) could be a dependence of light-induced degradation of p-i-n cells on the wavelength of the incident light. (Note that we are not suggesting that the Staebler-Wronski effect itself is wavelength-dependent). For example, if blue light were to cause more degradation than red light, then it would indeed be advantageous to remove the blue light in the thin and relatively stable top stack of a tandem device.

To test this idea, the J-V curves of single junction cells with 0.5μm i-layers were measured before and after 90 minutes (open-circuit) light soaking with blue and red light. For both wavelengths the intensity was adjusted to give a saturated current under reverse-bias equal to that produced under AM1.5 100 mW cm^{-2} illumination. The soaking light was derived from an ELH lamp in conjunction with either a short pass or a long pass filter, the cut-off wavelengths, being 480 nm and 630 nm, respectively. The entire experiment was performed twice (using distinct cells), once using an ELH (blue-deficient) source in order to acquire the J-V curves, and once using an HMI source. All cells were from the same run, and had an initial efficiency of about 8.5%. The results are shown in Table III.

Regardless of the light source used for J-V measurement, this data suggests that the degradation in p-i-n cells caused by red light is greater than that caused by blue light. A further subtle point is that the degradation itself depends on the spectrum of light used to measure the cell, and appears greater when a redder source is used. Contrary to what we were hoping to find, these results do not offer any additional reason for the greater stability of tandem cells.

Table III: Percent change in photovoltaic parameters of single junction cells after red and blue light soaks.

	ELH Source				HMI Source			
	V_{oc}	J_{sc}	FF	Eff	V_{oc}	J_{sc}	FF	Eff
Red Soak	-0.7	-4.4	-12.0	-16.5	+1.6	-4.4	-8.5	-11.1
Blue Soak	-1.9	-3.7	- 8.5	-13.6	+1.1	-4.8	-3.7	- 7.2

2.63 Effect of Non-Standard A-Si deposition Conditions

Another important issue concerns the dependence of cell efficiency and stability on i-layer deposition conditions. We have in the past made use of accelerated light soaking (ALS, performed on dots at high intensities) in order to rapidly assess different types of a-Si:H. Thus Fig. 12 shows ALS data (efficiency versus log soak time) for 0.3 and 0.5μm cells prepared under standard conditions, and three cells prepared under nonstandard conditions. Under these conditions (70 suns, 30 C) the nonstandard cells, although of initially lower efficiency, eventually out perform standard p-i-n cells.

In our semiannual report we categorized five types of relative stability that occur under ALS [3]. Fig. 13 shows the remarkable behavior of Type 1 cells: no significant degradation in V_{OC}, J_{SC}, or FF under ALS.

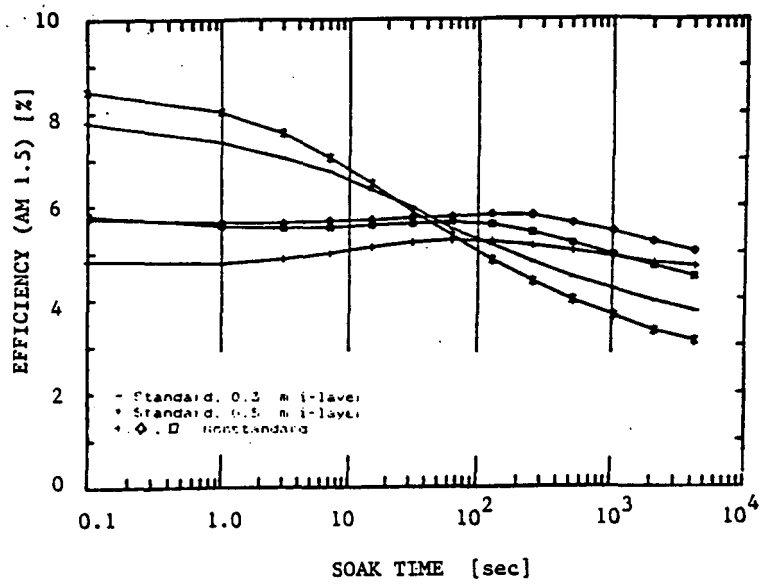

Fig. 12 Accelerated light soaking for variously-prepared p-i-n cells (standard conditions, 0.3μm and 0.5μm i-layer thickness; and 3 cells prepared under nonstandard conditions, 0.3μm i-layer thicknesses).

Detailed stability maps prepared for an entire 1 x 1 sq.ft. plate shows that several of the instability types can coexist in different regions on a single substrate. This degree of complexity was completely unexpected.

More recently, we found that qualitative results obtained under accelerated light soaking are not necessarily in agreement with those obtained near 1 sun irradiation. For example, some nonstandard cells show a significant increase in efficiency for the first several minutes of accelerated light soaking (earlier termed the Inverse Staebler-Wronski effect). Under 1 sun conditions, however, cells from the same run show a continuous drop

in efficiency. Further work in this area is clearly necessary, and our current feeling is that a dependable guide to stability can only be obtained by soaking under conditions as realistic as possible (see Section 2.61 above).

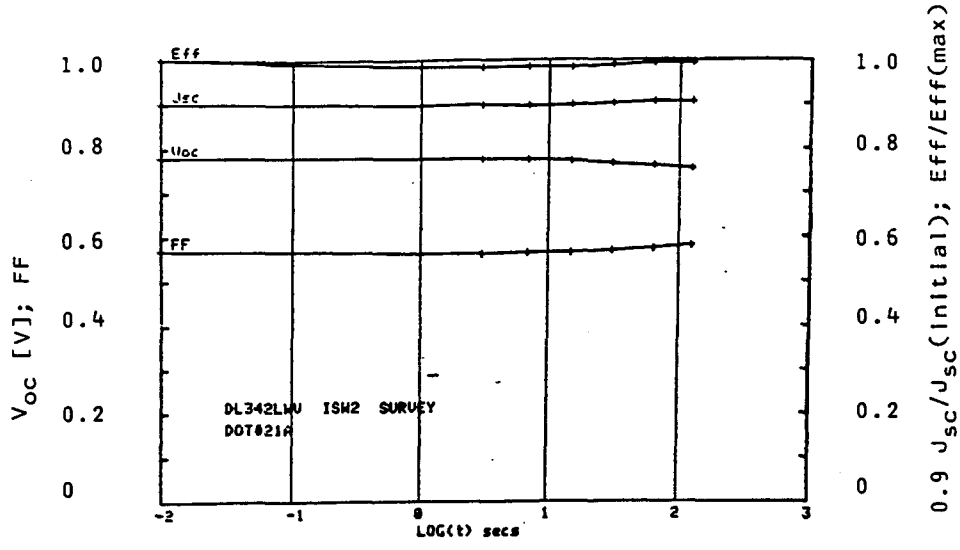

Fig. 13 Type 1 accelerated light-soak stability: no significant degradation in V_{OC}, J_{SC} or FF.

2.64 Thickness Dependence of Degradation of FF and J_{SC}

Experience had taught us that thick single junction cells suffer considerable loss in J_{SC} upon light soaking, while thinner cells do not. To study this more quantitatively, dots were light soaked at 10-40 suns and measured periodically at 1 sun using a computer controlled apparatus. Results were plotted against log time in the usual fashion. The data showed that the rate of decrease of fill factor and short circuit current with log time have different dependency on thickness. This is shown in Fig. 14. The percent drop *er decade of time for fill factor is constant at about 10%. However, the percent drop per decade for short circuit current increases strongly with film thickness. These data are not explained by any theory of the light soaking of p-i-n cells.

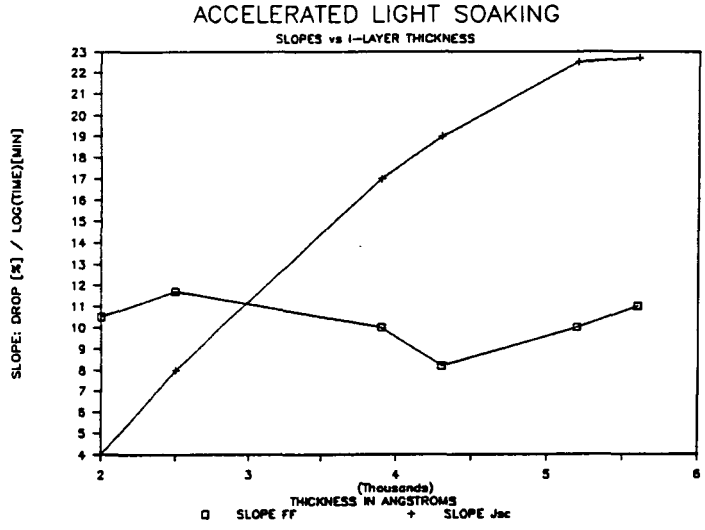

Fig. 14 Rate of decrease of FF and J_{SC} (% drop/log time (min)) versus i-layer thickness for accelerated light soaking

SECTION 3.0

NON-SEMICONDUCTOR MATERIALS

In keeping with our policy of critically examining and improving all layers and interfaces associated with a-Si:H devices in order to increase their conversion efficiency, we discuss below our efforts concerning non a-Si:H materials from the front of the cell to the back, namely the glass, the transparent conductor and its diffusion barrier, semiconducting metal oxide recombination layers, and conducting oxide based back reflectors.

3.1 GLASS

3.11 Antireflective (Graded Index) Glass Surfaces

We have produced antireflective layers on the surface of alkali-borosilicate (pyrex) glass by etching the heat-treated glass to form a porous surface layer (skeleton of silica) that possesses a graded index of refraction. The composition of the glass used is 81% SiO_2, 13% B_2O_3, 4% Na_2O, and 2% Al_2O_3. We have performed this treatment on glass pieces up to 1 ft.sq. The formation of the graded index surface layer is accomplished as follows:

1. heat to induce coarsening of the microphases i.e., phase separation (630°C for 3 hours, furnace cool).
2. etch to remove surface skin of silica-rich glass (10% ammonium bifluoride for 20 minutes)
3. rinse (distilled water for 30 seconds)
4. leach/etch at elevated temperature to preferentially attack non-silica component of the phase-separated glass (1% HF at 90 C for 5 minutes)
5. rinse (distilled water for 2 minutes, followed by alcohol)
6. dry

By these means we have obtained a reflectance (at 630nm) of 1%, and a transmittance of 99% for a plate of pyrex glass, the usual figures being 8% and 92%, respectively. The graded index surface layers are also effective in reducing reflection in the rear IR and at high angles of incidence. Fig. 15 shows an SEM micrograph of the treated glass surface.

3.12 Use of Graded Index Glass as a Substrate for Devices

In order to apply the above technique for producing antireflecting glass surfaces to PV panels, at least one surface of the glass must be treated and the opposite surface must be provided with the tin oxide coating. There are several ways in which this can be accomplished. One possible sequence is to heat and etch the glass (thereby forming a porous surface layer on both sides) and then coat the glass with tin oxide. This we

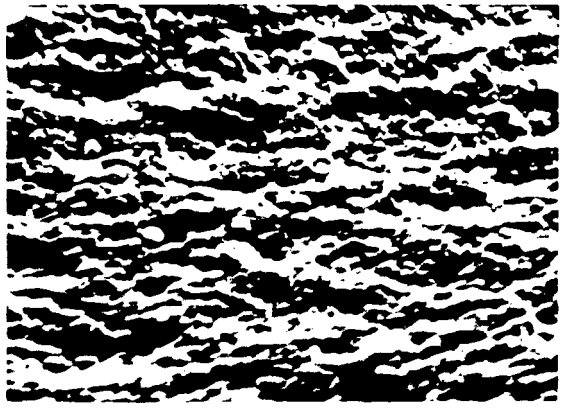

Fig. 15 SEM micrograph of alkali-borosilicate glass after formation of a graded-index surface layer (mag. 10kX, 60 tilt).

found yielded only 4.5% average conversion efficiency.

We therefore tried starting with SnO_2-coated glass, which was then treated and etched to form the graded index layer on the outer glass surface. Two single junction a-Si:H runs were performed using as substrates this glass and control pieces of either untreated pyrex or soda lime glass. In both runs an improvement in the optical performance of the cell was achieved through the use of the graded index glass, regardless of whether J_{SC}, peak quantum efficiency, or integrated current density parameters were examined. These results are shown in Table IV. We are unable to properly quantify this improvement at the present time since the improvement appeared to range from 3% to a high of 9%. The heat treatment of the glass/SnO_2 was found to increase the sheet resistance of the SnO_2, and this probably accounts for the higher R_S observed in the devices.

Table IV. Results of J-V and spectral response measurements on cells prepared on various glass substrates, some having a graded index surface layer as AR coating.

Plate #	Glass Type	V_{oc} (V)	J_{sc} (mA/cm^2)	FF	Eff (%)	R_s ohmcm^2	QE (peak)	J(int) (mA/cm^2)
DL332LWV	soda lime, untreated	0.825	15.5	0.634	8.13	7.05	0.773	13.4
DL332LEV	pyrex, graded	0.811	16.2	0.624	8.18	9.20	0.845	14.4
DL336LWV	pyrex, graded	0.812	15.9	0.588	7.95	9.83	0.777	13.7
DL336LEV	pyrex, untreated	0.770	15.3	0.572	6.76	9.67	0.757	12.8

Note: J(int) is the integrated current density predicted by spectral response measurements. It is the integral of the product of the external quantum efficiency and the AM1.5 global spectrum normalized to 100mW/cm^2.

In order to remedy this problem, the improved processing sequence i) heat treatment, ii) SnO_2 deposition, iii) etching, was devised. This was relatively successful, and transmittances of 83.5%, and 84.7% were measured for graded index pyrex/SnO_2 compared to 81.2% for untreated pyrex/SnO_2. The SnO_2 sheet resistance was unaffected by the etch. Tandem cell quantum efficiency data show that the peak QE for graded index pyrex is 0.79-0.80, compared to 0.76-0.77 for standard soda lime glass substrates. Quantum efficiency data for DL392 (graded index pyrex) is shown in Fig. 16.

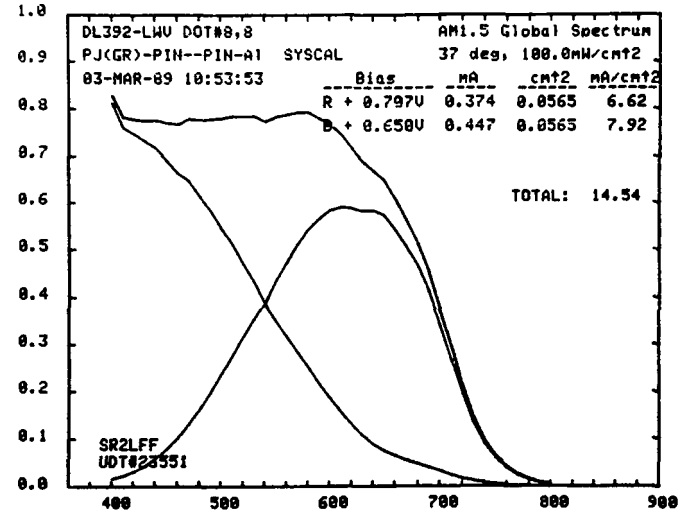

Fig. 16 External quantum efficiency of the top and bottom stacks of a tandem cell prepared on a glass/SnO_2 substrate having a graded-index AR surface layer.

Analysis of tandem cell J-V data indicates that the use of graded index glass/SnO_2 prepared in this manner leads to a slight reduction in V_{oc}, but a larger increase in J_{sc}, for a net gain in efficiency.

Even later work seemed to indicate that a variation on this last sequence, namely pre-etching of the silica-rich surface layer prior to SnO_2 deposition, could eliminate the drop in V_{oc}.

3.2 TRANSPARENT CONDUCTORS

In this subsection we discuss the chemical vapor deposition of SiO_2 barrier layers to improve the conductivity of fluorine-doped tin oxide, and the preparation of an alternative transparent conductor, zinc oxide, by one of several possible methods, namely RF magnetron sputtering. The availability of a new transparent conductor opens many exciting avenues for future research, including the lure of improved V_{oc}, J_{sc}, FF and stability.

3.21 Silicon Dioxide Barrier Layers for Tin Oxide

Our past work showed that a SiO_2 diffusion barrier reduces the diffusion of impurities, notably sodium, from soda lime glass into tin oxide during the growth of the SnO_2 from $SnCl_4$ at 500-600 C. Consequently the conductivity of the SnO_2 is much improved. We have extended this work by performing a detailed study of the deposition of SiO_2 thin films by atmospheric pressure chemical vapor deposition from 0.02-0.6 mol.% SiH_4 and 1-50 mol.% O_2 in N_2 [10]. Most of this work was performed in a belt-driven muffle furnace, and some in a two-zone tube furnace.

An annoying feature of this SiO_2 deposition scheme is powder formation. To study this, a glass rod was positioned down the center of the glass tube. Two sources of particle formation were observed: i) gas phase nucleation, which occurred roughly in the regions of maximum film growth rate, and ii) condensation of gas-phase species into microscopic particles whenever the temperature drops more than about 5 C. The latter source was always observed, and produced more powder than i). It appeared to be genuinely unavoidable, but because of thermophoresis, did not contaminate the SiO_2 film.

Large excess oxygen concentrations and the addition of propylene to suppress gas-phase reactions within the injector head were also investigated. We were interested in inhibiting gas-phase reactions near the bottom surface of the injector head in order to increase silane utilization and to produce thicker oxide layers.

We continue by examining the SiO_2 growth rate, the effect of SiO_2 thickness on SiO_2 conductivity. A discussion of the oxygen dependence, silane dependence, and uniformity of SiO_2 growth can be found in our semiannual report [3].

3.211 Silicon Dioxide Growth Rate

The growth rate depends on geometrical parameters, such as the distance between the injector slot and the substrate, as well as on flow rates, temperatures, and belt speed. The various effects on the growth rate were studied by measuring deposition profiles; as an example, Fig. 17 shows the growth rate as a function of distance from the injector slot for two different flow rates. Only half of the profile is shown, since the other half is essentially the mirror image.

One observes, under the deposition conditions indicated in Fig. 17, that the maximum growth rate does not occur directly under the injector head slot. Furthermore, as the flow rate approximately doubles, the distance from the slot at which the maximum growth occurs also approximately doubles. This suggest that the maximum film growth rate occurs at roughly the same gas-phase residence time. If the rate-limiting step involved surface reactions, then one would expect the position of the maximum growth rate to be independent of the flow rate and to be directly under the slot, since the substrate is already heated to the deposition temperature before entering the deposition area, and since the SiH_4 concentration is at its maximum at this position. The results shown in Fig. 17 are therefore consistent with depositions in which reactions in the gas phase determine the film growth rate.

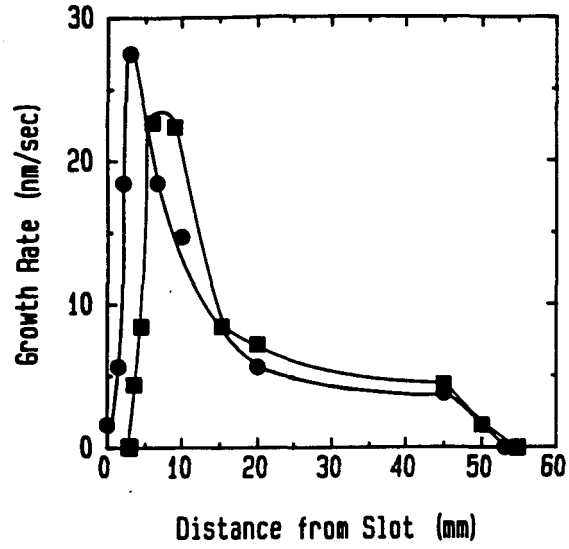

Fig. 17 Silicon dioxide film growth rate for a total flow rate of about 5.8 1/min (●) and 11.6 1/min (■). Injector head temperature 61 C, deposition temperature 573 C, gas mixture 0.28% SiH_4, 34% O_2, balance N_2.

The maximum SiO_2 film growth rate at several temperatures between about 469 C and 572 C was obtained from deposition profiles obtained for the same gas-phase concentration and flow rates. An arrhenius plot of these results is shown in Fig. 18. The activation energy for these deposition conditions is about 27 kJ/mole. At a temperature of 572 C and a belt speed of 30.5 cm/min, the film thickness was 200nm. Since the width of the deposition profile is 0-11cm, this corresponds to an average growth rate of 10nm/sec.

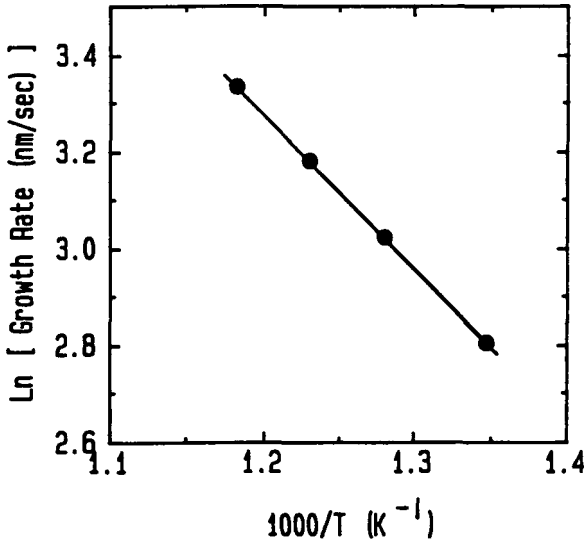

Fig. 18 Arrhenius plot for SiO_2 growth rates obtained between 469 C and 572 C.

3.212 Effect of SiO_2 on the Doping of Tin Oxide

Figures 19 and 20 show the conductivity of tin oxide samples 500-800nm thick on soda lime glass and on soda lime glass coated with silicon dioxide about 200-300nm thick, respectively, as a function of dopant flowrate.

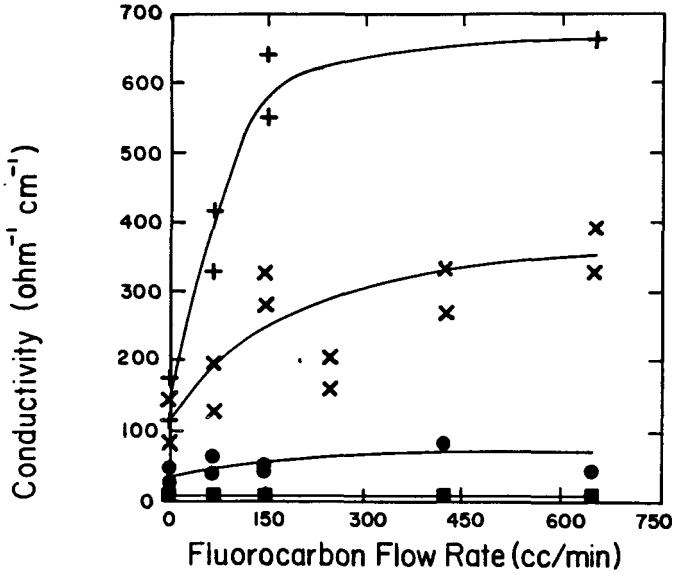

Fig. 19 Conductivity of F-doped tin oxide on soda lime glass as a function of deposition temperature and fluorocarbon flow rate. The curves are for 608 C(+), 584 C(x), 537 C(•), and 490 C (■).

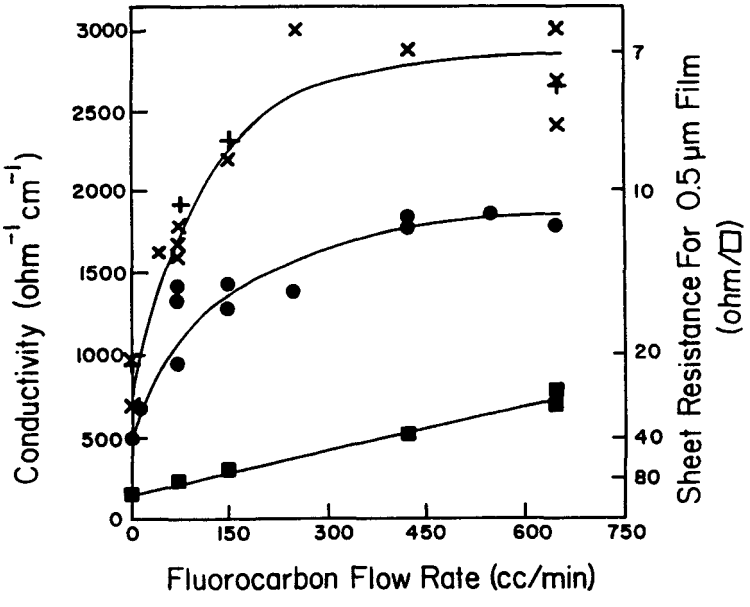

Fig. 20 Conductivity of F-doped tin oxide on 200-300nm SiO_2 on soda lime glass as a function of deposition temperature and fluorocarbon flow rate. The curves are for 608 C and 584 C(+) and (x), 537 (•) and 490 C (■).

In both cases, the tin oxide conductivity tends to increase and saturate (at a level dependent on deposition temperature) as the fluorine dopant flow rate is increased. At a given dopant flow rate, in both cases, the conductivity tends to improve as the deposition temperature is increased. However, under the same deposition conditions, one observes that the conductivities are about 4 to 100 times larger for the tin oxide deposited on the silicon dioxide. In fact, at a given temperature, the maximum conductivity on the uncoated glass is less than the minimum (undoped) conductivity of the tin oxide on the silicon dioxide coated glass. It also appears that the temperature for maximum conductivity saturates at a lower temperature on the coated glass since there is little difference between about 584 C and 608 C for the coated glass. In contrast, on the uncoated glass the higher temperature yields substantially higher conductivities except in the case of little or no dopant.

3.213 Dependence of Tin Oxide Conductivity on SiO_2 Thickness

The effectiveness of silicon dioxide as a diffusion barrier layer has been studied as a function of its thickness. First, thin 80-90nm tin oxide films were deposited with a fluorocarbon flow rate well below its conductivity saturation flow rate. As the tin oxide is deposited, the underlying tin oxide may to some extent serve as a diffusion barrier layer for the tin oxide being deposited. Thus, a thin coating of tin oxide is more sensitive to the effectiveness of the silicon dioxide layer. The low dopant flow was similarly chosen to increase the sensitivity of the tin oxide to differences in the barrier layers, since the slop of the conductivity versus the dopant flow is steeper for this flow. From curve (B) of Fig. 21, one notes that there is a rapid rise in the conductivity up to about 15nm thick silicon dioxide, thereafter there is more modest linear increase in the conductivity of the tin oxide up to at least about 250μm. Curve (A) is for tin oxide films 480-510nm thick and moderately doped. This curve is more representative of the situation encountered for solar cell applications. It is seen that only about 10nm of silicon dioxide are needed to obtain almost the full effectiveness of a 250nm barrier layer.

3.22 Zinc Oxide

High quality transparent conducting films of polycrystalline zinc oxide (ZnO) have been prepared with sheet resistances of 5 ohms/square for films less than 1μm in thickness. The films have been proven suitable for a-Si:H deposition and cell fabrication.

3.221 Deposition and Properties

The ZnO films were prepared by RF magnetron sputtering from a doped oxide target. A cryo-pumped, load-locked deposition system was employed, and the substrates (up to 1 ft.sq.) were unheated. The sputtering was performed in pure argon at 6 mTorr pressure; no additional oxygen was required. At 1kW RF power the deposition rate was 72nm/min (12 A/s). Fig. 22 shows a mapping of the sheet resistance across a 1 ft.sq. substrate. The average sheet resistance is 5.4 ohms/square. At the center of the plate the ZnO thickness was 0.75μm, and the resistivity 4.0 x 10^{-4} ohm cm (conductivity 2.0 x 10^{3} S cm^{-1}). Some variation across the plate both of thickness and conductivity were observed.

The transmission of the ZnO film at the center of the plate is shown in Fig. 23. From the absorption edge at 370-380nm we infer an energy gap of about 3.3 eV. This may

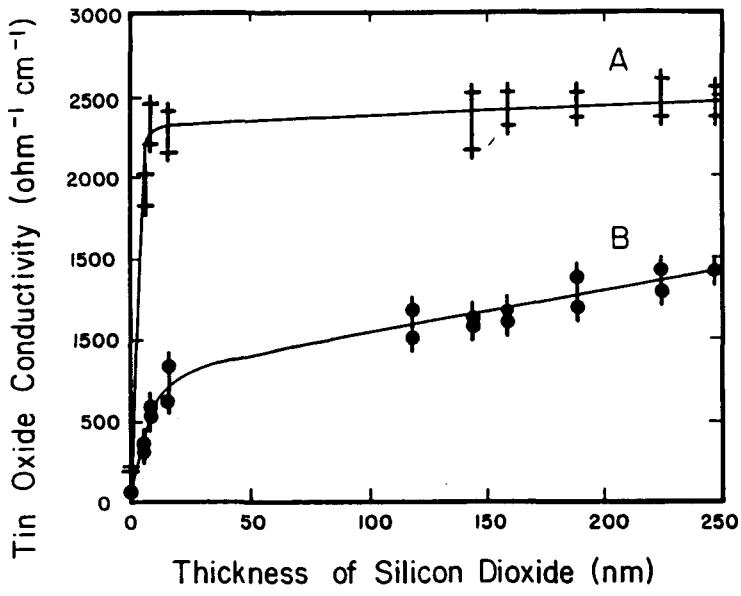

Fig. 21 Conductivity of tin oxide as a function of SiO_2 thickness. Curve A: 480-150nm tin oxide, curve B: 80-90nm tin oxide, fluorocarbon flow rates were 250 cc/min and 110cc/min, respectively.

shift slightly depending on the level of doping (Burstein-Moss effect). In the visible and near IR region of the spectrum the average transmission is about 90%. Beyond a wavelength of 2μm the transmission is essentially zero. We may estimate the carrier concentration N using the expression for the plasma frequency from Drude's model

$$\omega_p = \frac{Ne^2}{m^*\epsilon}$$

taking $m^* = 0.38m$, $\epsilon_r = n^2 = 4.9$, and $\omega_p = 1.5\mu m$ yields $N = 9 \times 10^{20}$ cm^{-3}. From the measured conductivity (2.5×10^3 S cm^{-1}) we can then calculate the mobility. This we find to be about 17 cm^2/Vs.

It has been our experience that sputtered ZnO films generally have a smooth, specular surface. In thicker films, however, some surface texture develops, as can be seen in the SEM micrograph of a 0.8μm ZnO film shown in Fig. 24.

3.222 ZnO as a Substrate for a-Si:H deposition

The use of ZnO as a substrate for a-Si:H cell deposition is not as straightforward as substituting ZnO-coated glass for SnO_2-coated glass. For example, in a standard tandem a-Si:H run these two substrates yielded average efficiencies of 4.3% and 7.8%, respectively. The ZnO substrate had both a low J_{sc} and FF. The low J_{sc} was attributed to the specular nature of the ZnO and the consequent absence of light trapping. The low FF we concluded was due to a ZnO/p-layer contact resistance. Although we were able to successfully circumvent the granularity problem by sputtering ZnO onto SnO_2-coated glass, thereby replicating the granularity of the SnO_2 and achieving an efficiency of 7.1%, it would of course be more desirable to prepare granular ZnO films directly. Further work solved the ZnO/p-layer contact resistance problem by means of

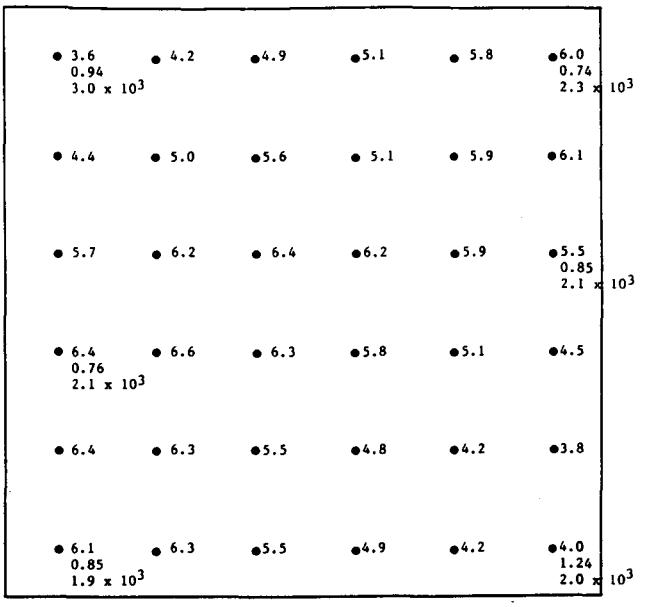

Fig. 22 Mapping of the sheet resistance (ohms/sq.) of ZnO across a 1 sq.ft. glass substrate. In addition, the thickness (μm) and conductivity (S/cm) are given in 6 locations.

surface treatment of the ZnO. Thus Fig. 25 shows the J-V curve of an 8.3% single junction cell formed on a glass/SnO_2/ZnO substrate after surface treatment.

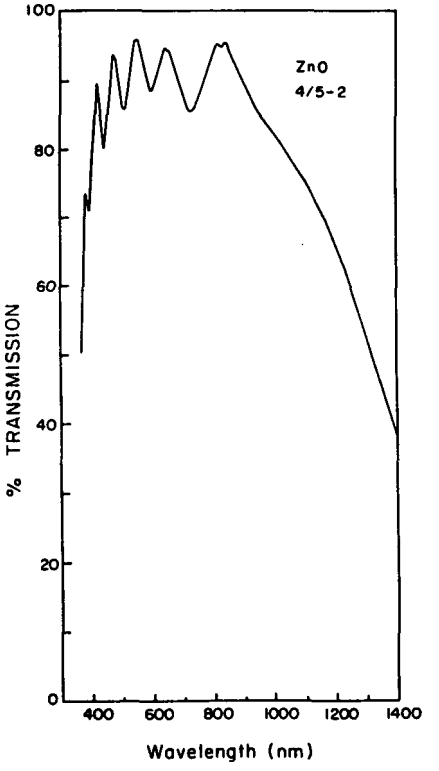

Fig. 23 Transmission versus wavelength for a doped ZnO film prepared by magnetron sputtering (thickness 0.75μm, sheet resistance 5.4 ohms/sq.).

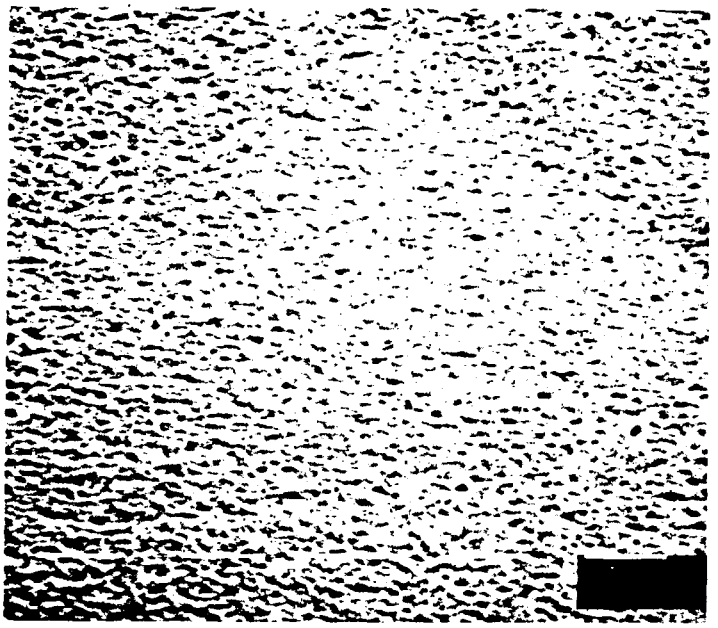

Fig. 24 SEM micrograph of a 0.8μm thick ZnO film.

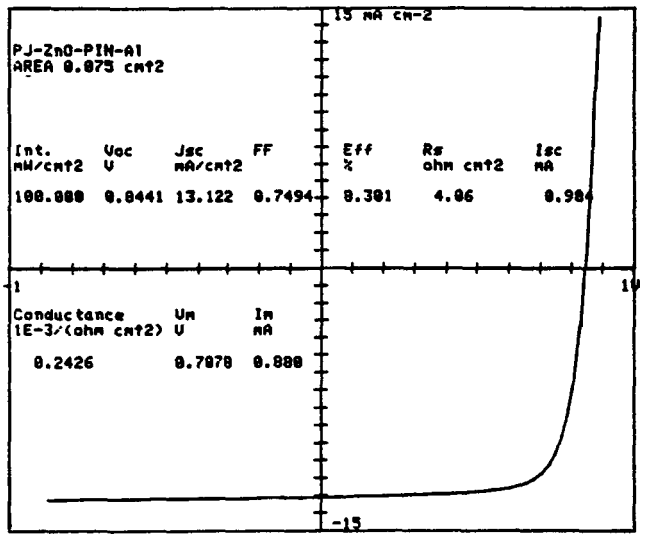

Fig. 25 J-V curve of an 8.3% p-i-n cell prepared on glass/SnO_2/ZnO.

3.3 SEMICONDUCTING METAL OXIDES

We have found that semiconducting metal oxides can be used to advantage as a recombination layer separating the two stacks of tandem cells. The use of the TiO_x in this role has already been described in Section 2. Here we describe the deposition of this layer. The TiO_x films were prepared by thermal evaporation of titanium sesquioxide, Ti_2O_3, a sub-oxide of Ti. Deposition rates between 0.3 and 2 A/s were employed, and the substrate was unheated. The room temperature electrical conductivity of this material was 2.2×10^{-6} ohm^{-1} cm^{-1}, although we discovered that a factor of 100 improvement in the conductivity could be obtained by hydrogen plasma treatment.

3.4 BACK REFLECTORS

In order to achieve effective light trapping of weakly absorbed light in a p-i-n cell, the cell must be metallized in such a way as to achieve a high optical reflectivity for the a-Si/contact layer system. This is needed in order to sustain a large number of light passes through the i-layer. Since evaporated Ag contacts are unreliable, we have concentrated on bi-layer reflectors of the form sputtered, conducting metal oxide/metal (or other reflector).

3.41 Indium Tin Oxide Based Reflectors

Good optical performance was achieved for back reflectors of the form ITO/Ag, leading to increased J_{sc} in cells as a result of improved red response. As i-layers were made thinner it appeared that most of the current could be recovered through switching from Al to ITO/Ag metallization. Thus, current gains were roughly 1mA/cm^2 for an i-layer thickness of 0.5μm, 1.9 mA/cm^2 for 0.3μm, and 3.3 mA/cm^2 for 0.25μm. Quantum efficiencies of 0.50 at a wavelength of 700nm were achieved using a 0.5μm i-layer and ITO/Ag reflector, as shown in Fig. 26. Metallization of tandem cell DL312 gave top and bottom stack integrated currents of 6.44 and 6.32 mA/cm^2 with Al, and 6.63 and 7.42 mA/cm^2 with ITO/Ag.

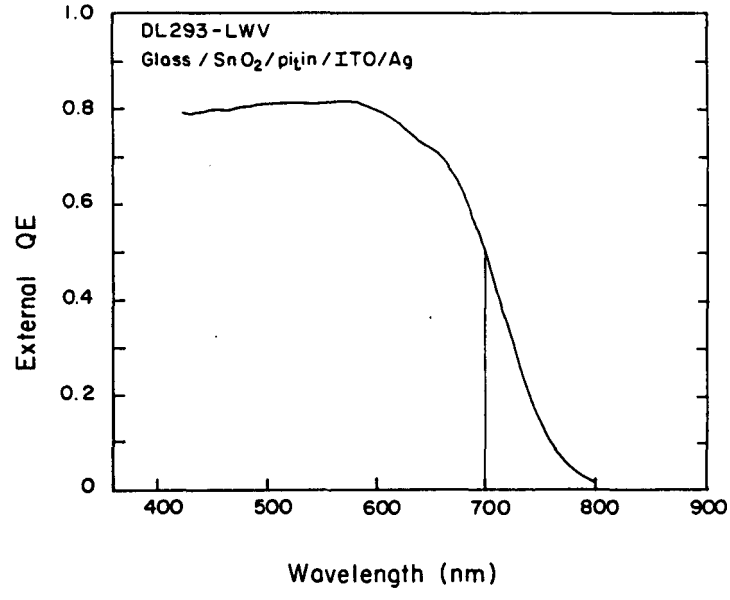

Fig. 26 External quantum efficiency versus wavelength for a p-i-n cell employing a carbon-graded p-layer and ITO/Ag back reflector.

Despite the gains in J_{SC}, cell efficiencies with ITO/Ag were usually lower because of a 2% drop in V_{OC} and 4-15% drop in FF. Many attempts were made to solve the drop in FF problem, but without complete success. Introduction of a Ti barrier between the n-layer and ITO did indeed fully regain the FF, but even 30A Ti proved too absorbing and reduced J_{SC} by 1.6 mA/cm^2. Definite improvements in FF were obtained by employing a p-i-n-p structure, but metallization with Al still gave a higher FF than that obtained with ITO. The FF problem was discussed at greater length in our semiannual report [3].

For these reasons we decided to try an alternative transparent conductor, namely ZnO.

3.42 Zinc Oxide Based Reflectors

Experiments have been performed using ZnO, ZnO/Al, ZnO/Cu, ZnO/Ag, and ZnO/$BaSO_4$ reflective metallization. Improved red response and increased J_{SC} are always observed, while FF is usually slightly lower than for Al, although not always so. We do not yet know what control FF. Table V summarizes spectral response data obtained for tandem cell DL406 as a function of the type of back reflector. The following observations were made:

1. Cells metallized with ZnO plus a reflector (eg barium sulphate or Cu) possess much better red response than cells metallized with a single layer of Al or ZnO.

2. Addition of the barium sulphate to ZnO increased QE(700nm) from 0.33 to 0.48, and the same of the top and bottom stack current densities from 13.2 to 14.4 mA/cm^2. ZnO/Cu appears slightly inferior (optically) to ZnO/$BaSO_4$.

3. ZnO/Cu appears slightly inferior (optically) to ZnO/$BaSO_4$.

The spectral response of cell DL406LEV-A#5 with a QE(700nm) of 48% (ZnO/$BaSO_4$ contact) is shown in Fig. 27. With ZnO/Cu metallization, we have measured 0.08 cm^2 tandem cells from this run at 9.1% efficiency (1.66V, 8.09 mA/cm^2, FF 0.678). Work on ZnO-based reflectors is continuing.

Table V. Spectral response data for cells from run DL406 with different back reflectors.

	Al (LW)	ZnO (LEV-A#5)	ZnO/$BaSO_4$ (LEV-A#5)	ZnO/Cu (LEV-A#2)	ZnO/Cu (LEV-B)
J_{top}	7.31	6.93	7.09	6.86	7.19
J_{bottom}	6.51	6.23	7.32	7.35	7.48
J_{top} + J_{bottom}	13.82	13.16	14.41	14.21	14.67
QE(700nm) t+b	0.31	0.33	0.48	0.42	0.40

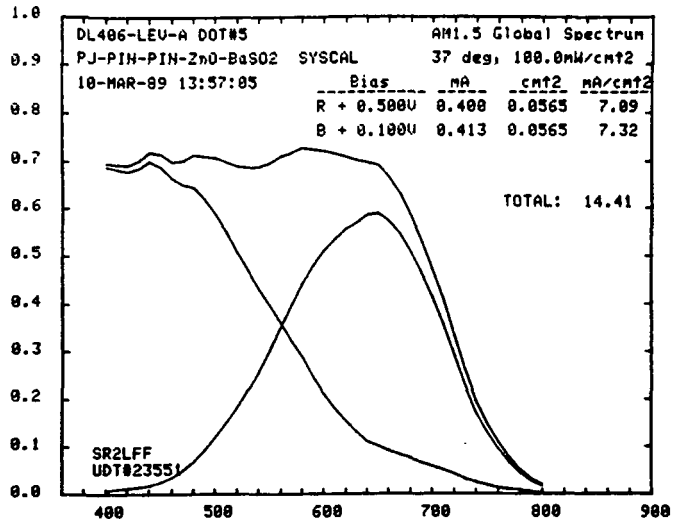

Fig. 27 External quantum efficiency of the top and bottom stacks of a tandem cell employing a ZnO/barium sulphate back reflector.

SECTION 4.0

SUBMODULES

The principal objective here is to fabricate submodules having conversion efficiencies that approach as closely as possible the intrinsic, small area cell efficiency. This requires that the numerous sources of power loss first be identified, and then their effect minimized through appropriate processing changes. Novel submodule designs described below offer theoretically higher efficiencies than the standard three-scribe submodule, but are more complex to fabricate. A further important objective is to achieve the highest possible long term efficiency by controlling light induced degradation and eliminating material or contact-related degradation phenomena.

4.1 HIGHEST PERFORMANCE SUBMODULES

Submodule research has been carried out using both 1x1 sq.ft. and 1x3 sq.ft. SnO_2- coated glass substrates. The parameters and performance of the best submodules produced in the current reporting period in these sizes are shown in Table VI.

Notable progress has been made in the area of tandem junction submodules; during the second half of Phase II submodule power output increased from 14.6 watts to 15.8 watts for 1x3 sq.ft. panels, and from 5.3 watts to 6.0 watts for 1x1 sq.ft. panels. The 6.0 watt tandem panel had an active area efficiency of 7.66% (aperture area efficiency 7.2%) and was prepared on 10 ohm/sq. tin oxide. Its J-V curve is shown in Fig. 28. A 60A TiO_x recombination layer separated the two stacks, and contributed to the high V_{oc} of 48.3V. This represents an average voltage per cell of 1.67V.

Double width (2cm wide) cells were employed in the 15.8 watt 1x3 sq.ft. tandem submodule in order to maintain a V_{oc} near 23V. Unfortunately, the gain in active area

was offset by increased resistive losses in the tin oxide, the latter accounting for the low FF of this submodule.

The 5.9 watt single junction panel was prepared on 5 ohm/sq. tin oxide. In this run, hydrogen plasmas were struck both before and after p-layer deposition.

Table VI. Record 1 x 1 sq.ft. and 1 x 3 sq.ft. submodules produced during Phase II

	Single Junction		Tandem Junction	
Run #	DL366REV		DL380RWV	
Active Area (cm^2)	806		789	
Aperture Area (cm^2)	842		842	
Number of cells	29		29	
Sheet Resistance of SnO_2 (ohms/sq.)	5		10	
	Chronar	SERI	Chronar	SERI
Open Circuit Voltage(V)	23.9	23.6	48.3	47.8
Short Circuit Current(mA)	378.4	360	189.	191
Current Density (mA/cm^2) (active area basis)	13.6	---	6.95	---
Fill Factor (%)	65.7	67.0	66.1	65.0
Power (W)	5.93*	5.68	6.04**	5.89
Efficiency, active area (%)		---	7.66	---
Efficiency, aperture area (%)	7.04	6.8	7.17	7.0

	Single Junction	Tandem Junction
	Chronar	Chronar
Active Area (cm^2)	2360	2360
Aperture Area (cm^2)	2787	2545
Number of cells	29	14
Open Circuit Voltage(V)	23.6	23.1
Short Circuit Current(mA)	1182	1170
Current Density (mA/cm^2) (active area basis)	14.5	6.94
Fill Factor (%)	63.6	58.4
Power (W)	17.75	15.78
Efficiency, active area (%)	7.52	6.69
Efficiency, aperture area (%)	6.36	6.20

*5.84W prior to defect elimination (2nd stage)
**5.66W prior to defect elimination (2nd stage)

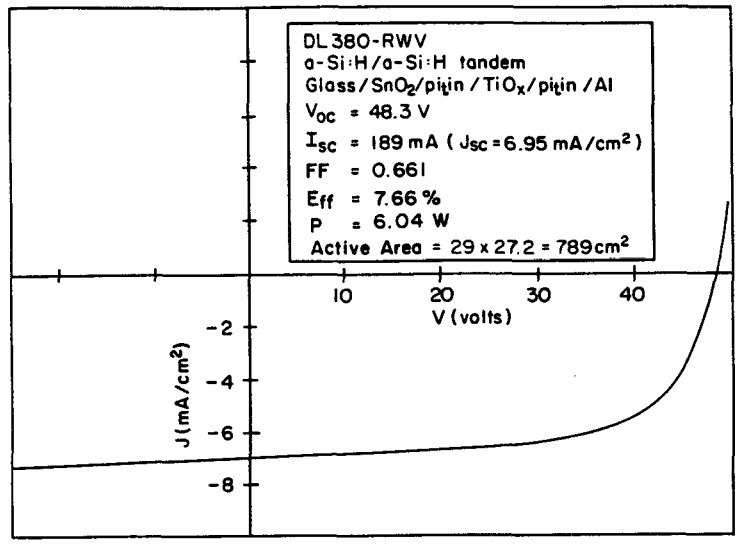

Fig. 28 J-V curve for a 1sq.ft. a-Si:H/a-Si:H tandem submodule (29 cells). The submodule has an active area efficiency of 7.7% and generates 6.0 watts.

4.2 FACTORS IDENTIFIED AS CONTRIBUTING TO POWER LOSS

We have identified the following factors that, to a greater or lesser degree, can contribute to power loss in submodules.

1. Nonuniformity of a-Si:H cell efficiency across the plate, the causes being:

   a. variation in a-Si:H thickness and properties

   b. variation in SnO_2 sheet resistance, including substantially higher values near the edge

2. Run-to-run variability in a-Si:H cell performance. Possible causes are: dopant retention, ambient conditions, SnO_2 surface, deposition control, leaks, especially in dopant shut-off valves.

3. Sheet resistance losses in the SnO_2

4. Inactive areas occupied by cell-cell interconnects

5. Intercell contact resistance, caused by:

   a. Inadequate removal of Si at the Si patterning step (laser preferable to mechanical scribing). This in turn may be related to:

      1) drift in laser tuning
      2) changes in p layer thickness or properties
      3) varition in i-layer thickness and properties

b. Poor metallization. Possible causes are:

1) pressure too high, contaminants present such as water vapor or hydrocarbons
2) contamination of scribe region prior to metallization
3) Al layer too thin, leading to poor step coverage
4) contamination of Al source material (or tungsten coils)

6. Localized defects, including:

a. shunt-type defects from laser scribing
b. a-Si pinholes
c. scratches in the a-Si caused by rough handling, especially when plate is mounted in the metallizer
d. miscellaneous other defects (see below)

7. Poor n-layer/Al contact, caused by:

a. oxide growth on a-Si (or other contamination) due to excessive time (and/or improper storage) between Si deposition and metallization.
b. poor metallization; quality of the first 20Å of deposit is crucial.

Several of these problems are addressed at greater length below. These areas include a categorization of localized defects, and steps that can be taken to remove some of them, questions of uniformity, laser patterning issues, and finally, SnO_2 losses and questions of active area, which are addressed by new module designs.

4.21 Localized Defects

We have identified 7 types of localized defect that impair submodule performance. The defect types are:

1. Classic pinhole. This occurs in the a-Si:H and is caused most often by Si flakes or other debris.

2. Laser induced. Caused by imperfect green laser isolation of the Al.

3. Al bridging. Caused by debris or dust masking the beam during green laser isolation.

4. SnO_2 laser isolation. A relatively uncommon defect in which the a-Si:H over the SnO_2 scribe edge is sensitive to abrasion, resulting in shorts to the Al. Caused by defective laser optics.

5. Defect area. This type of defect can occupy an area up to several cm^2, with no discernible mechanical feature observable under an optical microscope. It possesses a peculiar sensitivity to shunt spreading, and may be related to tin oxide morphology.

6. Al spits. Spitting of Al during evaporation is an intermittent problem that can be handled by proper current control.

7. Scattered singularity. These are isolated defects that exist in numerous localities through the cell. The defects are very small, with no visible structure, but because of their large number, they seriously reduce cell isolation.

The number of defects per panel ranges from just a few to around 50. When the laser isolation process is working well, most defects are of type 1 or 5.

4.22 Defect Elimination

We have devised means for post-fabrication elimination of several types of shunting defects. In order to quantify shunting in a panel, and so gauge the effectiveness of these procedures, we have introduced a quantity termed the "ceiling average" resistance. We define this quantity below, and then proceed to describe and illustrate the removal of defects.

4.221 Definition of Ceiling Average Shunt Resistance

In evaluating the submodule performance a"ceiling average" resistance is introduced as a measure of shunting in the panel. Shunting may occur within each series-connected cell, as well as across the interconnect. The shunting (isolation) resistance is measured, in the dark, as the resistance between the Al layers of two adjacent cells. The ceiling value is given by the minimum shunt resistance for which the power loss remains below about 3%. for a 1x1 sq.ft. panel made up of 29 single-junction cells, the ceiling value is 100 ohm, for a correspondence tandem-junction panel it is 400 ohm. The "ceiling average" is found by measuring the shunting resistance between all cells, counting all values above the ceiling only as 100 or 400 ohm, respectively, whereas those below as the measured value, and by calculating the average of all these values. This average value reflects the quality of the panel, even if only a few cells are shunted; the normal average would not, since even totally shorted cells would be outweighed by sufficiently high shunt resistance of the other cells.

4.222 Defect Elimination: Methods and Examples

The first method is a routine procedure for "current blasting" individual series-connected cells in order to improve their isolation resistance. In this technique, each cell is momentarily reverse biased at several volts in order to remove certain types of shunts. Table VII shows the dramatic effect on V_{OC} that can result from this treatment in some instances. In addition, the ceiling average isolation resistance increased from 286 Ω to 317 Ω, and the efficiency from 5.1 to 6.1%. The current blasting was performed at a voltage of -5V.

The second method (which we term "shunt busting") is based on the observation of small hot spots when the panel is biased, and their subsequent removal using Al etchant. Table VIII illustrates how the full potential performance of the a-Si:H on a given panel can be realized (subject to the constraints of active area, uniformity, and SnO_2 resistance) through the application of these two techniques. In this example, performed on a tandem 1 x 1 sq.ft. submodule, current blasting at -5V increased the ceiling average isolation resistance from 275 to 319 ohms, accompanied by an increase in efficiency from 6.06% to 6.52%, while the subsequent chemical method further raised the ceiling average

to 399 ohms and the (active area) efficiency to 7.48%. During the latter process 15 pinholes were eliminated and one small area of laser-induced shunting was mended. It

Table VII. Effect of current blasting on the photovoltaic parameters and ceiling average isolation resistance for a tandem panel.

	Before	After
V_{oc} (V)	34.8	40.4
J_{sc} (mA/cm^2)	7.05	7.08
FF (%)	60.6	61.6
Eff (%)	5.13	6.08
P (W)	4.03	4.78
Ceiling Av. Resistance (Ω)	286	317

Table VIII. Performance of 1 ft^2 tandem submodule DL373-REV at various stages of defect elimination Final power output 6 watts.

Elimination step	V_{oc} (V)	I_{sc} (mA)	J_{sc} (mA/cm^2)	FF (%)	Eff (%)	R_{isol}[a] (Ω)	N[b]	Power (W)
A. Initial measurement	43.2	195	7.07	57.6	6.06	275	11	4.85
B. Electrical	45.3	194	7.03	59.3	6.52	319	7	5.22
C. Chemical	47.1	196	7.11	64.3	7.42	390	1 (122)	5.94
D. Chemical	47.1	197	7.14	64.5	7.48	399	1 (362)	5.99

Defect elimination step		Percent improvement V_{oc}	FF
Electrical	(A - B)	5%	3%
Chemical	(B - D)	4%	9%
Total	(A - D)	9%	12%

a) R_{isol}: ceiling average; see text.

b) N: number of cells with isolation <400 ohms.

appears that current blasting tends to improve V_{oc}, while the second stage (shunt busting) tends to improve fill factor. Similar techniques were employed for the 6 watt submodule in Fig. 28.

4.23 Submodule Analysis

The existence of non-uniformities in panel construction was demonstrated by eliminating a 1" border round plate DL380REV and scaling the measured power output to the full panel area. Thus, for the entire panel (aperture area 851 cm^2) 5.8 watts was obtained, while for the central 10" x 10" section (exact aperture area 610 cm^2) 4.46 watts was obtained, which scales to 6.22 watts for a full panel. We deduce that the power density for the central region is 7.31 mW/cm^2, but only 5.56 mW/cm^2 for the 241 cm^2 border region, i.e. 24% lower. The average power density for the entire plate is 6.82 mW/cm^2, i.e. 6.7% lower than that of the central section. The active area efficiency of the interconnected cells (without border) was 7.7%. The average dot efficiency for the LW plate was 8.04%. We may therefore prepare the following table (Table IX) illustrating the contributions to efficiency loss in passing from the dot to the entire square foot panel. Also included in the Table are data for a single junction panel. It is instructive to note that the sheet resistance of the SnO_2 (10 ohms/sq.) has a much larger effect in dropping the dot efficiency to that of the interconnect for single junction cells than tandem cells. For both types of panels the loss in efficiency near the border is about the same.

Table IX. Module efficiency versus dot efficiency: loss analysis for two particular runs, one tandem, one single junction.

	Tandem DL380REV	Single DL259REV	Reason for drop
Average dot efficiency	8.04%	8.97%	
Interconnected cell efficiency (active area, border excluded)	7.70%	7.82%	R_s, Rc
Interconnected cell efficiency (aperture area, border excluded)	7.31%	7.00%	Dead area
Interconnected cell efficiency (aperture area, full plate)	6.82%	6.62%	Edge effects

R_s - denotes SnO_2 sheet resistance
Rc - denotes Al-SnO_2 contact resistance
Dead area - area lost to interconnects
Edge effects - refers to the lower output border regions

4.3 NEW LOW-LOSS DESIGNS FOR SUBMODULES

Conventional modules, in which the SnO_2, a-Si:H, and Al are each laser scribed after deposition in order to accomplish cell interconnection, suffer significant losses both in active area and I^2R loss in the transparent conductor. We have shown that the total loss can be greatly reduced by employing radically different schemes for contacting the SnO_2 and interconnecting the cells [3,11,12]. One of the new schemes, termed the dot contact interconnect scheme, consumes almost no active area in effecting the cell-cell interconnections. This type of module utilizes two levels of metallization separated by an insulator. It further offers great flexibility in choice of output current and voltage combinations for a given panel size, since the width of the unit cell is not limited by the sheet resistance of the transparent conductor.

The dot contact module design is shown in plan view in Fig. 29. After sequential deposition of the SnO_2/a-Si/Al_1 layers, laser patterning is employed to cut through all three layers to form the unit cells. Next, an array of holes is etched through the a-Si/Al_1 layers to expose the underlying SnO_2. Exposed portions of the Al_1 layer are then insulated, and a second layer of Al is deposited in order to a) pick up multiple dot contact with the exposed SnO_2, and b) interconnect the unit cells through an Al_1/Al_2 contact; the Al_2 layer can be patterned by simple masking. In order to minimize losses, the dots should be arranged in a hexagonal array, as indicated in Fig. 29.

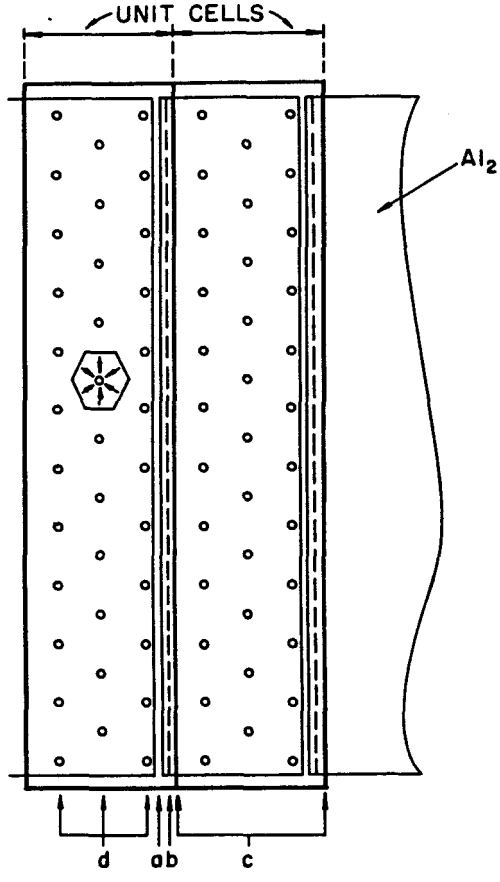

Fig. 29 Plan view of a dot contact module showing the unit cells, and Al_2 layer as though transparent. Note hexagonal current collection region around the dot contacts. a: Al_2 patterning, b: insulator scribe (to allow Al_2/Al_1 interconnect), c: unit cell scribe (through SnO_2/a-Si/Al_1), d: three rows of dot contacts (Al_2-SnO_2 contact).

A further perspective on this design is provided by a direct comparison of losses for dot contact modules and conventional laser-patterned modules optimized for 1 sun operation. Some results of these calculations are given in Table X. The sheet resistance of the transparent conductor was assumed to be 10 ohms/sq., a scribe width of

Table X. Comparison of losses for dot contact modules and conventional modules.

Type of Cell	Cell width (cm)	Contact area (%)	Area loss due to scribes (%)	Area loss due to dots (%)	I^2R loss (%)	Total losses (%)
Tandem Junction						
dot contact, r_1=0.05cm						
10 rows of dots	7.45	1.2	0.1	1.2	0.9	2.3
1 row of dots	0.74	1.2	1.3	1.2	0.9	3.5
conventional, s=0.05cm	1.07	0.9	4.5	---	2.3	6.8
Single Junction						
dot contact, r_1=0.05cm						
10 rows of dots	5.50	2.2	0.2	2.2	1.6	4.0
1 row of dots	0.55	2.2	1.8	2.2	1.6	5.6
conventional, s=0.05cm	0.67	1.5	6.9	---	3.7	10.7

0.1 mm was assumed for the dot contact module, and a total dead width s = 0.5 mm was assumed for the three scribes of the conventional module. The results are quite striking - the dot geometry is capable of reducing total module losses stemming from inactive area and I^2R losses in the transparent conductor by a factor of 2-3.

Exploratory work has confirmed the feasibility of fabricating dot contact modules. A short-circuit current of 0.88A was obtained from a single, tandem junction dot contact cell of area 124 cm^2, while a 929 cm^2 submodule consisting of 6 unit cells, each containing 50 0.25 cm diameter dot contacts, had an aperture area of 867 cm^2, and an aperture area utilization of 98.1%.

4.4 LONG TERM OUTDOOR TESTING
(This section updated in early June, 1989)

Long term outdoor data for a glass-encapsulated 929 cm^2 (1 ft^2) tandem submodule having a 0.4μm i_2-layer is shown in Fig. 30. The submodule was periodically brought indoors for measurement under standard conditions; while outdoors it was kept on load close to its maximum power point. Over a period of 271 days, an overall loss of output of 13% was observed. This data clearly has a seasonal component, the increased module temperature in the spring and early summer of 1989 leading to a partial annealing of defects. Regrettably, module temperature was not continuously monitored, but a measurement (in sunlight) on June 2, 1989 revealed a temperature of 68C. This presumably accounts for the smaller drop in efficiency observed in the outdoor test than in the indoor study of Table II. Further work is necessary to accurately describe the effect of module temperature on long term stability behavior.

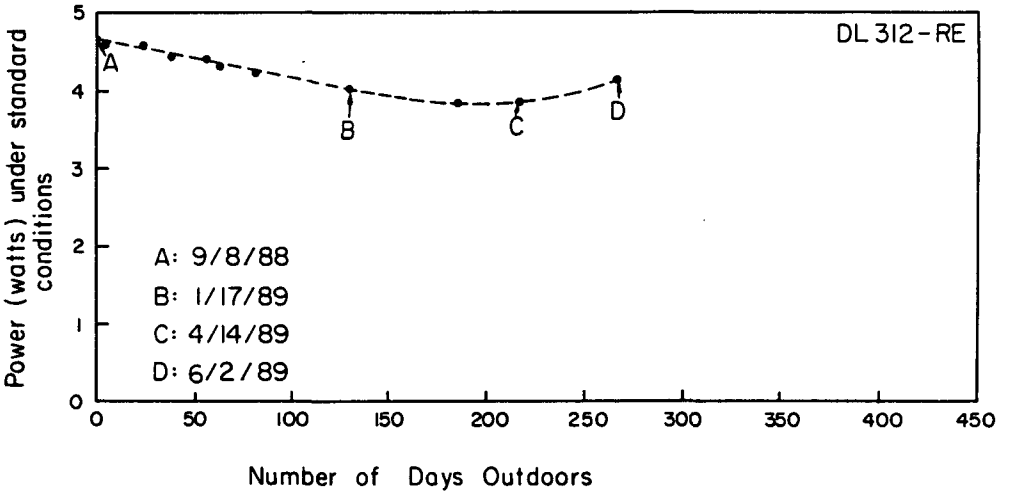

Fig. 30 Power output under standard conditions for a glass-encapsulated tandem submodule as a function of outdoor exposure time.

SECTION 5.0

REFERENCES

1. A.E. Delahoy et al., Phase I Semi-Annual Technical Progress Report for the period March 16, 1987 - September 30, 1987, Subcontract No. ZB-7-06003-1.

2. H. Schade, A.E. Delahoy, Proc. 8th E.C. Photovoltaic Solar Energy Conference (I. Solomon, B. Equer, P. Helm, Eds.) Kluwer Academic Publishers, Dordrecht 1988, p. 756.

3. A.E. Delahoy et al., Phase II Semi-Annual Technical Progress Report for the period March 16, 1988 - September 30, 1988, Subcontract No. ZB-7-06003-1.

4. R.S. Crandall, K. Sadlon, J. Kalina, and A.E. Delahoy, presented at the MRS Spring Meeting, 1989.

5. D. Ritter, E. Zeldov, and K. Weiser, Appl. Phys. Lett., 49, 791 (1986).

6. I. Balberg, A.E. Delahoy, and H.A. Weakliem, Appl. Phys. Lett., 53, 992 (1988).

7. I. Balberg, A.E. Delahoy, and H.A. Weakliem, Proc. 20th IEEE Photovoltaic Specialists Conference, 1988 pp. 352-356.

8. I. Balberg, A.E. Delahoy, and H.A. Weakliem, Appl. Phys. Lett., 53, 1949 (1988).

9. A.E. Delahoy, T. Tonon, J.A. Cambridge, M. Johnson, L. Michalski, F.J. Kampas, Proc. 8th E.C. Photovoltaic Solar Energy Conference (I. Solomon, B. Equer, P. Helm, Eds.) Kluwer Academic Publishers, Dordrecht 1988, p. 646.

10. F.B. Ellis, Jr., and J. Houghton, J. Mater. Res. in press.

11. A.E. Delahoy, U.S. Patent allowed.

12. A.E. Delahoy, to be presented at the SERI PV AR&D 9th. Review Meeting, Lakewood, CO, May 1989, and to be published in Solar Cells.

Document Control Page	1. SERI Report No. SERI/STR-211-3609	2. NTIS Accession No. DE89009515	3. Recipient's Accession No.

4. Title and Subtitle
Research on Amorpnous Silicon Based Thin Film Photovoltaic Devices, Task B: Research on Stable High-Efficiency, Large Area Amorphous Silicon Based Submodules

5. Publication Date
December 1989

6.

7. Author(s)
A.E. Delahoy, F.B. Ellis, Jr., F.J. Kampas, T. Tronan, H.A. Weakliem

8. Performing Organization Rept. No.

9. Performing Organization Name and Address
Chronar Corporation
PO Box 177
Princeton, New Jersey 08542

10. Project/Task/Work Unit No.

11. Contract (C) or Grant (G) No.
(C) ZB-7-06003-1
(G)

12. Sponsoring Organization Name and Address
Solar Energy Research Institute
1617 Cole Boulevard
Golden, Colorado 80401-3393

13. Type of Report & Period Covered
Annual Technical Report

14. 3/16/88 - 3/15/89

15. Supplementary Notes
SERI Technical Monitor: W. Luft, (303) 231-1823

16. Abstract (Limit: 200 words)

This report describes a project to develop amorphous silicon p-i-n/p-i-n tandem junction photovoltaic submodules with an aperture-area efficiency of at least 9%. A second objective was to demonstrate 8%-efficient tandem submodules that degrade by no more than 5% under standard light-soaking conditions. Improved deposition conditions were established for tandem cells; the resulting efficiencies were nearly as high as those for single-junction cells. An amorphous silicon tandem cell (1 ft^2) was fabricated with an aperture-area efficiency of 7.2%. Also, good outdoor stability was observed for a glass-encapsulated tandem submodule. Also produced (by magnetron sputtering) were high-quality doped zinc-oxide films (5 ohms/square).

17. Document Analysis
a. Descriptors Photovoltaics ; thin films ; amorphous silicon submodules ; efficiency

b. Identifiers/Open-Ended Terms

c. UC Categories 271

18. Availability Statement
National Technical Information Service
U.S. Department of Commerce
5285 Port Royal Road
Springfield, Virginia 22161

19. No. of Pages
51

20. Price
A04

Form No. 0069 (3-25-82)